Semaphorin7A patterns neural circuitry in the lateral line of the zebrafish

Agnik Dasgupta[1,*], Caleb C. Reagor[1,2], Sang P. Paik[1,3], Lauren M. Snow[1,4], Adrian Jacobo[1,5], and A. J. Hudspeth[1,]

[1] Howard Hughes Medical Institute and Laboratory of Sensory Neuroscience, The Rockefeller University, New York, NY, USA

*Corresponding author: Dr. Agnik Dasgupta
Laboratory of Sensory Neuroscience
The Rockefeller University
New York, NY 10065
Telephone: 212-327-7353
E-mail: adasgupta@rockefeller.edu

[2] Tri-Institutional PhD Program in Computational Biology and Medicine, New York, NY, USA

[3] Present address: Department of Functional Neuroanatomy, Institute for Anatomy and Cell Biology, Heidelberg University, Heidelberg, Germany

[4] Present address: Brigham and Women's Hospital, Boston, MA, USA

[5]Chan Zuckerberg Biohub San Francisco, San Francisco, CA, USA

Abstract

In a developing nervous system, axonal arbors often undergo complex rearrangements before neural circuits attain their final innervation topology. In the lateral line sensory system of the zebrafish, developing sensory axons reorganize their terminal arborization patterns to establish precise neural microcircuits around the mechanosensory hair cells. However, a quantitative understanding of the changes in the sensory arbor morphology and the regulators behind the microcircuit assembly remain enigmatic. Here, we report that Semaphorin7A (Sema7A) acts as an important mediator of these processes. Utilizing a semi-automated three-dimensional neurite tracing methodology and computational techniques, we have identified and quantitatively analyzed distinct topological features that shape the network in wild-type and Sema7A loss-of-function mutants. In contrast to those of wild-type animals, the sensory axons in Sema7A mutants display aberrant arborizations with disorganized network topology and diminished contacts to hair cells. Moreover, ectopic expression of a secreted form of Sema7A by non-hair cells induces chemotropic guidance of sensory axons. Our findings demonstrate that Sema7A functions both as a juxtracrine and as a secreted cue to pattern neural circuitry during sensory organ development.

Introduction

Pathfinding axons are directed to their appropriate synaptic targets by a variety of guidance cues. While approaching or traversing the target field, the growth cones of migrating axons encounter secreted or cell surface-attached ligands and respond by steering toward or away from their sources (1–4). Fine-grained control of these factors is critical for the establishment of proper neural circuitry.

The zebrafish's lateral line provides a tractable *in vivo* system for exploring the mechanisms that guide the assembly of neural circuits in a peripheral nervous system. In particular, it is possible to detect individual hair cells and the sensory axons that innervate them throughout the first week of development (5). The primary posterior lateral line on each side of the zebrafish's tail consists of about seven neuromasts, which contain mechanoreceptive hair

46 cells of opposing polarities—half sensitive to headward (rostrad) water motion and the
47 complementary half to tailward (caudad) water motion—that cluster at their centers (6). The
48 sensory axons of the lateral-line nerve branch, arborize, and consolidate around the basolateral
49 surfaces of the hair cells (Figure 1A). To aid in an animal's swimming behavior, these hair cells
50 sense water currents and relay signals to the brain through the sensory axons (7). The well-
51 defined structure of the ramifications and synaptic contacts of the sensory axons highlight the
52 need to determine the molecular signals behind the assembly of such precise microcircuits (8).
53 We adopted a candidate-gene strategy to seek factors that direct the growth of afferent
54 growth cones in the zebrafish's lateral line. Analysis of single-cell RNA sequencing data
55 identified the *semaphorin7a* (*sema7a*) gene to be highly expressed in hair cells of that organ
56 (9). Semaphorins are important regulators of axonal growth and target finding during the
57 patterning of diverse neural circuits (10). The semaphorin family includes proteins that are
58 secreted, transmembrane, and cell surface-attached (11). Among these, Semaphorin7A
59 (Sema7A) is the only molecule that is anchored to the outer leaflet of the lipid bilayer of the cell
60 membrane by a glycosylphosphatidylinositol (GPI) linker (11). Unlike many other semaphorins,
61 which act as repulsive cues (12,13), Sema7A is involved in promoting axon growth (4) and
62 imparting directional signals by interacting with the integrin and plexin families of receptors
63 residing on the pathfinding axons (14–16). Sema7A likely occurs *in vivo* in both GPI-anchored
64 and soluble forms (17–19), and studies of neuronal explants confirm that both forms can induce
65 directed axonal outgrowth (4). Furthermore, it has been proposed that the GPI anchor is
66 cleaved by membrane-resident GPI-specific phospholipases (GPI-PLs) or matrix
67 metalloproteases to release the Sema7A into the extracellular environment and thus regulate
68 dynamic cellular processes (20,21). Because these observations indicate that Sema7A might
69 influence neuronal development both as a juxtracrine and as a diffusive signal, we investigated
70 the role of Sema7A in sculpting a vertebrate peripheral sensory organ.

71 **Results**

72 **Sema7A expression and localization in hair cells.** The zebrafish genome contains a single
73 *sema7a* gene that produces two transcripts. One transcript encodes Sema7A-GPI, a full-
74 length, GPI-linked, cell surface-attached protein. The second transcript yields Sema7A^{sec}, a
75 protein with a truncated C-terminus, which we conjecture is secreted into the local environment.
76 Each transcript encodes an N-terminal signal sequence and a single copy of the conserved
77 sema domain (11). Using primers that flank the regions encoding the sema domain and the
78 distinct C-termini of the two transcripts, we performed reverse transcription and polymerase
79 chain reactions (RT-PCR) to identify both the membrane-anchored and the secreted transcript
80 in developing larvae (Figure 1B; Figure 1—figure supplement 1A). Single-cell RNA sequencing
81 data also have shown that the *sema7a* transcript is particularly enriched in the immature and
82 mature hair cells of the neuromast during early larval development (9), a period when sensory
83 axons of the posterior lateral line contact hair cells and form synapses with them (5,22). Indeed,
84 we have observed Sema7A to be specifically localized in both mature and immature hair cells
85 (Figure 1C; Figure 1—figure supplement 1B-E).

86 As neuromasts mature, the contacts between sensory axons and hair cells increase in
87 number, become stabilized, and establish synapses (5,22). Because Sema7A can modulate
88 axon guidance (4,14) and synapse formation (15), we wondered whether the level of Sema7A
89 also changes during neuromast development. Upon quantifying the average intensity of
90 Sema7A, we found similar expression in rostrally and caudally polarized hair cells of
91 neuromasts at 1.5, 2, 3, and 4 days post fertilization (dpf). The average Sema7A intensity
92 increased significantly over this period in both rostrally and caudally polarized hair cells. At
93 1.5 dpf, the neuromasts harbor primarily immature hair cells that make minimal contacts with
94 sensory axons and do not form stable association with axonal terminals (22). At this stage the
95 average Sema7A intensity in hair cells remained low. By 2-4 dpf the hair cells mature to form
96 stable contacts and well-defined synapses with the sensory axons (5,23). The average
97 Sema7A intensity in hair cells at each of these stages rose to levels that significantly exceeded
98 those of 1.5 dpf neuromasts (Figure 1D). This rise in the amount of Sema7A during neuromast

99 maturation supports a role for Sema7A in the guidance of sensory axons and their interaction
100 with hair cells.

101 We additionally demonstrated an anisotropic distribution of Sema7A along the
102 apicobasal axis of each hair cell. As neuromasts develop through 2, 3, and 4 dpf, Sema7A
103 remained highly enriched in the subapical region of the hair cell, the site of the Golgi network.
104 This localization suggests that Sema7A—like other proteins of the semaphorin family (24)—is
105 directed to the plasmalemma through Golgi-mediated vesicular trafficking. While Sema7A
106 maintained a high level in the subapical region, the protein increasingly accumulated at the
107 base of the hair cell: the Sema7A level at the hair cell base was low at 2 dpf, but increased
108 sharply by 3 dpf and 4 dpf (Figure 1E; Figure 1—figure supplement 1F, G). During this period
109 the hair cells increase in number and mature, whereas the associated sensory axons arborize
110 to contact multiple hair cells and form robust synaptic boutons at their bases (5,23). The
111 progressive enrichment of Sema7A at the hair cell base and sensory-axon interface (Figure 1E,
112 F; Video 1) suggests that Sema7A acts as a mediator of contacts between sensory axons and
113 hair cells.

114 **Sema7A restricts sensory axons around clustered hair cells**. If Sema7A guides and
115 restricts the sensory arbors at and around the hair cells clustered in a neuromast, then
116 inactivating Sema7A function should disrupt this process. To test this hypothesis, we obtained
117 a *sema7a* mutant allele (*sema7a*^{sa24691}) with a point mutation that introduces a premature stop
118 codon in the conserved sema domain (Figure 2—figure supplement 1A). The homozygous
119 mutant, hereafter designated *sema7a*$^{-/-}$, should lack both the secreted and the membrane-
120 attached forms of Sema7A. The average intensity of Sema7A immunolabeling in hair cells
121 diminished by 61% in *sema7a*$^{-/-}$ larvae (0.34 ± 0.01 arbitrary units) in comparison to controls
122 (0.87 ± 0.01 arbitrary units). In a few cases we observed minute accumulations of Sema7A at
123 the subapical region, but little or no protein at the base of the mutant hair cells (Figure 2A;
124 Figure 2—figure supplement 1B).

125 To characterize the impact of the *sema7a*$^{-/-}$ mutation on arbor patterning, we utilized
126 doubly labeled transgenic fish *Tg(myo6b:actb1-EGFP;neurod1:tdTomato)* that marked the hair

127 cells and the sensory axons of the posterior lateral line with distinct fluorophores (25). In control
128 neuromasts, the sensory axons approached, arborized, and consolidated around the bases of
129 clustered hair cells (Figure 2B). Although the sensory axons approached the hair cells of
130 *sema7a*$^{-/-}$ neuromasts, they displayed aberrant arborization patterns with wayward projections
131 that extended transversely to the organ (Figure 2C). To quantitatively analyze the arborization
132 morphology, we traced the sensory arbors in three dimensions to generate skeletonized
133 network traces that depict–as pseudocolored trajectories–the increase in arbor length from the
134 point of arborization (Figure 2D, E).

135 To visualize the hair cell clusters and associated arborization networks from multiple
136 neuromasts, we aligned images of hair cell clusters, registered them at their hair bundles, from
137 neuromasts at 2 dpf, 3 dpf, and 4 dpf. Throughout development, the arborization networks of
138 control neuromasts largely remained within the contours of the hair cell clusters; the few that
139 reached farther nonetheless lingered nearby (Figure 2F). This result suggests that an attractive
140 cue retained the axons near the sensory organ. In *sema7a*$^{-/-}$ neuromasts, however the neuronal
141 arbors failed to consolidate within the boundaries of hair cell clusters and extended far beyond
142 them (Figure 2G; Figure 2—figure supplement 1C-H; Video 2).

143 We quantified the distribution of the sensory arbors around the center of the combined
144 hair cell clusters. For both the control and the *sema7a*$^{-/-}$ neuromasts, the arbor densities peaked
145 proximal to the boundaries of the hair cell clusters. Beyond the cluster boundaries, in control
146 neuromasts at 2 dpf, 3 dpf, and 4 dpf the arbor densities fell sharply at respectively 31.7 μm,
147 36.6 μm, and 32.7 μm from the center. In *sema7a*$^{-/-}$ neuromasts of the same ages, the sensory
148 arbors extended respectively 38.5 μm, 51.4 μm, and 56.6 μm from the center (Figure 2H;
149 Figure 2—figure supplement 1I, J; Figure 2—figure supplement 2A). Furthermore, we
150 quantified the degree of contact of the sensory arbors to their hair cell clusters in individual
151 neuromasts from both control and *sema7a*$^{-/-}$ mutants. In control neuromasts, the degree of
152 contact was 83 ± 1 % (mean ± SEM) at 2 dpf and 84 ± 1 % at 3 dpf, but significantly increased
153 to 90 ± 1 % at 4 dpf (Figure 2I; Figure 2—figure supplement 2B). This observation indicates
154 that the sensory arbors reinforce their association to the hair cell clusters as neuromasts

155 develop. However, in *sema7a*$^{-/-}$ neuromasts such contact was significantly reduced. Only
156 69 ± 4 % of sensory arbors at 2 dpf were closely associated with the corresponding hair cell
157 clusters, a value that remained at 67 ± 2 % at both 3 dpf and 4 dpf (Figure 2I). These findings
158 signify that, with simultaneous disruption of both signaling modalities of Sema7A, the organ
159 fails to restrict the localization of sensory arbors and has significantly diminished contact with
160 them.

161 **Sema7A patterns the arborization network's topology.** Accurate spatial arrangement of the
162 neuronal projections around hair cells is essential for proper retrieval and transmission of
163 sensory information. Mutations that perturb proper assembly of sensory neuronal microcircuits
164 lead to hearing impairment (26). Quantitative insight into the wiring pattern is therefore essential
165 to identify systematic aberrations in the microcircuit arising from genetic deficits. The three-
166 dimensional skeletonized network traces allowed us to accurately delineate the microcircuit
167 topology across individuals, developmental stages, and genotypes from living animals (Figure
168 2D, E). To quantitatively analyze the arbor network, we defined five topological attributes: (1)
169 nodes, denoted as junctions where arbors branch, converge, or cross; (2) loops, comprising
170 minimal arbor cycles forming topological holes; (3) bare terminals, defined as arbors with free
171 ends; (4) the node degree, calculated as the number of first-neighbor nodes incident to a node;
172 and (5) the arbor curvature, measured as the total curvature of a bare terminal (Figure 3A). We
173 quantified these attributes to accurately determine how the circuit topology is established
174 during maturation of the sensory organ in control larvae and how it is impacted by *sema7a*
175 deficit.

176 To determine how internode connectivity is distributed across networks, we quantified
177 the distribution of node degrees along the relative height of the hair cell cluster across
178 individuals, developmental stages, and genotypes. As for most other real-world networks (27),
179 we observed a highly skewed node-degree distribution: the majority of nodes had low node
180 degrees (three and four) and a small number of nodes—often acting as hubs, like the
181 arborization initiation point—had high node degrees (five to seven). The node degree varied
182 from three to seven in control larvae and three to six in *sema7a*$^{-/-}$ larvae. Across

183 developmental stages and genotypes, the high node degrees primarily occurred at the base
184 (region from 0 % to 10 % of the cluster height) of the hair cell cluster and acted as hubs for
185 the majority of branching events. Low node degrees primarily occurred along the basolateral
186 region (region from 10 % to 60 % of the cluster height) of the hair cell cluster. The apical region
187 (region from 60 % to 100 % of the cluster height) was sparsely populated with low node
188 degrees. The network's hierarchical organization along the organ's axis suggests that arbors
189 receive sensory inputs at multiple levels, allowing the network to carry out robust neural
190 computations. Even though nodes of low degree were most prevalent between genotypes
191 across developmental stages, their distribution along the relative organ axis became
192 significantly different at 4 dpf, with nodes in control larvae localized higher along the axis than
193 in *sema7a*$^{-/-}$ larvae (Figure 3A; Figure 3—figure supplement 1A-C; Table 1). These
194 observations indicate that Sema7A regulates both the spatial organization and node-degree
195 complexity of the sensory arbor network.

196 An average of 9.3 sensory axonal branches approach the hair cell cluster of a neuromast
197 (8). Pathfinding of sensory axons around the hair cell cluster results in the formation of axonal
198 fascicles that form numerous loops and bare terminals, which determine the microcircuit
199 topology (Figure 2B, D) (8). To optimally surround and contact the hair cell cluster, do the
200 sensory arbors prefer to adopt one topological feature over the other? To address this
201 question, we measured the correlation between the number of bare terminals and the number
202 of loops across individuals, developmental stages, and genotypes. In both 2 dpf and 3 dpf
203 larvae, the distributions remained highly scattered across individuals and genotypes.
204 However, by 4 dpf in the control larvae the arbor network contained either a high number of
205 loops with a low number of bare terminals or a high number of bare terminals with a low
206 number of loops. This result suggests that the stereotypical circuit topology observed in the
207 mature organ emerges from distinct events in which individual arbors transition from forming
208 bare terminals to forming closed loops encircling topological holes. That we did not observe a
209 similar transition in *sema7a*$^{-/-}$ neuromasts of the same age suggests that Sema7A regulates

210 the switch between these two distinct topological features (Figure 3B; Figure 3—figure
211 supplement 1D, E; Table 1).

212 Measurement of the contour length of both bare terminals and loops additionally
213 revealed that across developmental stages in control larvae the sensory arbors followed a
214 three-step process to choose the appropriate topological feature: arbors shorter than 10 μm
215 always formed bare terminals; arbors between 10 μm and 30 μm began to switch between
216 features, with arbors longer than 20 μm strongly preferring to form loops; and arbors longer
217 than 30 μm always formed loops. These results imply that the switch between bare terminals
218 and loops is partly dependent on the length of the arbors. However, this characteristic
219 topological preference was significantly perturbed in the *sema7a*$^{-/-}$ larvae across
220 developmental stages, as many of the sensory arbors longer than 30 μm remained as bare
221 terminals (Figure 3C; Figure 3—figure supplement 1F, G; Table 1). Furthermore, in 4 dpf
222 control neuromasts the majority of the loops contained four nodes and utilized 30-40 μm of
223 arbors to form closed cycles. These conserved topological attributes were significantly
224 perturbed in the *sema7a*$^{-/-}$ larvae of same age (Figure 3D, E; Figure 3—figure supplement
225 2A-D; Table 1). These findings indicate that Sema7A tightly regulates the sensory arbor loop
226 formation, including the preferred loop length and number of nodes per loop, to properly
227 surround and contact the hair cell cluster.

228 As observed previously, bare terminals in control neuromasts project transverse to the
229 organ and linger nearby, often curving back to form new loops and contact the hair cell cluster
230 (Figure 2D, F). To analyze the propensity of the bare terminals to curl backward, we measured
231 their total curvatures, defined as the sum of the curvature at each point along the length of an
232 arbor. Henceforth, we address the total curvature as the curvature of a bare terminal. We
233 classified the bare terminals in two categories: high-curvature arbors with curled morphology
234 and curvature greater than $\pi/6$ (30 degrees); and low-curvature arbors with linear morphology
235 and curvature less than $\pi/6$. In control neuromasts 44.8 % of arbors had low curvature
236 compared to 56.4 % in *sema7a*$^{-/-}$ neuromasts at 4 dpf. Concomitantly, 55.2 % of arbors had
237 high curvature in control neuromasts compared to 43.6 % in *sema7a*$^{-/-}$ neuromasts at 4 dpf

238 (Figure 3F; Figure 3—figure supplement 2E, F; Table 1). These observations further confirm
239 our hypothesis that a Sema7A-mediated attractive cue is involved in orienting bare neural
240 arbors toward the hair cell cluster to potentially form loops.

241 In summary, we propose that Sema7A regulates four key aspects of the topology of the
242 arborization network: (1) the node degree complexity along the organ's axis; (2) the transition
243 of arbors from bare terminals to loops; (3) the preference for forming loops containing four
244 nodes with 30-40 μm of arbors; and (4) the preference of bare terminals to adopt higher
245 curvature.

246 **Sema7A^{sec} is a sufficient chemoattractive cue for sensory axon guidance**. Because
247 genetic inactivation of the *sema7a* gene disrupts both signaling modalities of the cognate
248 protein, we could not assess the specific activity of the Sema7A^{sec} diffusive cue in guiding
249 lateral-line sensory axons. To independently verify the potential role of that isoform, we
250 therefore expressed the secreted variant ectopically and investigated the resultant arborization
251 patterns.

252 Analysis of the microcircuit connectivity of the neuromasts has demonstrated bare
253 sensory-axonal terminals in the perisynaptic compartments, where they do not contact the hair
254 cell membrane (8). We speculate that these bare terminals are attracted by a Sema7A^{sec}
255 diffusive cue. To test this hypothesis, we ectopically expressed Sema7A^{sec} protein tagged with
256 the fluorophore mKate2, then analyzed its effect on the morphology of sensory arbors.
257 Fertilized one-cell embryos were injected with the *hsp70:sema7a^{sec}-mKate2* plasmid and
258 raised to 3 dpf. Larvae expressing the transgenesis marker—the lens-specific red fluorescent
259 protein mCherry—were heat-shocked, incubated to allow expression, and subsequently
260 mounted for live imaging. In these larvae, a random mosaic of cells—often embryonic muscle
261 progenitors in the dermomyotome or mature myofibers—expressed the exogenous
262 Sema7A^{sec}-mKate2 protein. We selected only those neuromasts in which an ectopic integration
263 had occurred near the network of sensory arbors (Figure 4A,B). In all 22 such cases, we
264 observed robust axonal projections from the sensory arbor network toward the ectopically
265 expressing Sema7A^{sec} cells. When the exogenous *sema7a^{sec}* integration occurred in

266 embryonic muscle progenitor cells, which reside in a superficial layer external to the muscle
267 fibers and adjacent to the larval skin (28), the projections were able to form direct contacts with
268 them (Figure 4C; Videos 3, 4). But more often, when mature myofibers expressed the
269 exogenous Sema7A^{sec} deep in the myotome, the axonal projections approached those targets
270 but failed to contact them (Figure 4D, Videos 5, 6). This behavior likely arose because other
271 components in the myotomal niche—including the fibrous epimysium, other myofibers,
272 myoblasts, and immature myotubes whose surroundings are permeable to diverse diffusive
273 cues (29)—physically obstructed direct interaction of the extended neurites with the ectopically
274 expressing myofibers. All 18 of the injected but not heat-shocked control larvae did not express
275 ectopic Sema7A^{sec}, and we did not observe aberrant projections from the sensory arbor
276 network (Figure 4E).

277 To measure the accuracy of the extended axonal projections in finding the ectopic
278 Sema7A^{sec} source, we defined three parameters: (1) the source path, denoted as the linear
279 distance from the point of arborization to the boundary of an ectopically expressing Sema7A^{sec}
280 cell; (2) the projection path, representing the linear distance from the point of arborization to
281 the terminus of the extended projection; and (3) the projection proximity, calculated as the
282 linear distance from the terminus of the extended axonal projection to the nearest boundary of
283 the ectopically expressing Sema7A^{sec} cell (Figure 4B). We quantified these parameters from
284 18 of the 22 mosaic integration events; in the remainder the extended axonal projections–
285 although following the ectopic source–reentered the posterior lateral-line nerve so that
286 identification of the axon terminals was not possible (Figure 4—figure supplement 1A-A";
287 Video 7). When we plotted the projection path length against the source-path length, we
288 observed a nearly perfect correlation (Figure 4F). This result signifies that irrespective of the
289 location of the ectopic source–whether proximal or distal to the sensory arbor network–the
290 Sema7A^{sec} cue sufficed to attract axonal terminals from the sensory arbor. Furthermore, the
291 low average projection-proximity length of $3.5 \pm 0.7\ \mu$m (mean ± SEM) indicated that the
292 extended projection terminals remained either in contact (8 of 18) or in the vicinity (10 of 18) of

293 the ectopic Sema7A^{sec} sources (Figure 4G). These observations together demonstrate that the
294 Sema7A^{sec} diffusive cue is sufficient to provide neural guidance *in vivo*.
295 As the posterior lateral-line ganglion matures, newly formed neurons extend their axonal
296 growth cones along the posterior lateral-line nerve to reach the neuromasts (30). We wondered
297 whether the axonal projections that had yet to be associated with a neuromast could also
298 respond to an ectopic source of Sema7A^{sec}. Indeed, on five occasions in which *sema7a^{sec}*
299 integration had occurred between two neuromasts, we detected neurite extensions from the
300 posterior lateral-line nerve to the ectopic Sema7A^{sec} source (Figure 4—figure
301 supplement 1B-B"; Videos 8-10). The responsiveness of the posterior lateral-line axons to
302 Sema7A^{sec} might therefore be an intrinsic property of the neurons that does not require the
303 neuromast microenvironment.

304 **Sema7A deficiency impacts synaptic assembly.** Contact stabilization between an axon and
305 its target cell is essential for synapse formation (31). Neural GPI-anchored proteins can act as
306 regulators of various synaptic-adhesion pathways (32). In the mouse olfactory system, GPI-
307 anchored Sema7A is enriched in olfactory sensory axons and mediates sustained interaction
308 with the dendrites of mitral and tufted cells in the olfactory bulb to establish synapses (15). In
309 the developing mouse brain–particularly in Purkinje cells–GPI-anchored Sema7A instead
310 regulates the elimination of synapses onto climbing fibers (33). The role of anchored Sema7A
311 in regulating synaptic architecture can thus vary according to the cell type and developmental
312 stage. Our demonstration that Sema7A is necessary to consolidate the contact between
313 sensory axons and hair cells during neuromast development suggests a possible role in
314 regulating synaptic structure.
315 Proper synaptogenesis requires the correct spatial organization of the presynaptic and
316 postsynaptic apparatus at the apposition of two cells. At the interface between hair cells and
317 sensory axons, the synaptic network involves two scaffolding proteins in particular: ribeye, a
318 major constituent of the presynaptic ribbons (34), and membrane-associated guanylate kinase
319 (MAGUK), a conserved group of proteins that organize postsynaptic densities (35). Utilizing
320 these scaffolding proteins as markers, we investigated the impact of the *sema7a$^{-/-}$* mutation on

synapse formation. To analyze the distribution of presynaptic densities–immunolabeled with an antibody against the ribeye-associated presynaptic constituent C-terminal binding protein (CTBP) (34)–we counted the number and measured the area of CTBP punctae from multiple neuromasts at several stages of neuromast development (Figure 5A, B). The CTBP punctae in each hair cell ranged from zero to seven across developmental stages. In the zebrafish's posterior lateral line, the formation of presynaptic ribbons is an intrinsic property of the hair cells that does not require contact with lateral-line sensory axons. However, sustained contact with the sensory axon influences the maintenance and stability of ribbons (36). As neuromasts matured from 2 dpf to 4 dpf, we identified similar distribution patterns with a characteristic increase in the number of CTBP punctae in both control and *sema7a*$^{-/-}$ larvae (Figure 5C, D). This result implies that the formation of new presynaptic ribbons is not perturbed in the mutants, even though there are on average fewer CTBP punctae (Figure 5—figure supplement 1A-C). Measurement of the areas of CTBP punctae also showed similar distributions in both genotypes (Figure 5E, F) but the average area of presynaptic densities was reduced in the mutants (Figure 5—figure supplement 1D-F).

Because GPI-anchored Sema7A lacks a cytosolic domain, it is unlikely that Sema7A signaling directly induces formation of presynaptic ribbons. Instead, GPI-anchored Sema7A might induce postsynaptic assembly on the apposed neuronal membrane (15). To characterize the distribution of the postsynaptic aggregates–immunostained with a pan-MAGUK antibody–we performed analyses similar to those above (Figure 5I, J). At 4 dpf, 68.3 % of the hair cells in the control neuromasts were associated with at least one MAGUK punctum. In the *sema7a*$^{-/-}$ mutant this value fell to 37.5 % (Figure 5K, L). The average number of MAGUK punctae also declined in the mutants (Figure 5—figure supplement 1G-I). As control neuromasts matured from 2 dpf to 4 dpf, the MAGUK punctae showed a shift toward smaller sizes, suggesting that the postsynaptic structure fragmented into smaller entities as observed in other excitatory synapses (37). At 4 dpf, 77.5 % of the hair cells in the control neuromasts had postsynaptic densities with areas between 0.10 μm^2 and 0.40 μm^2. In the *sema7a*$^{-/-}$ mutant the corresponding value was only 42.5 % (Fig. 4M,N). The average area of MAGUK punctae

349 was also reduced in the mutants compared to the controls (Figure 5—figure supplement 1J-L**).**
350 We speculate that the abnormalities in postsynaptic structure arose from reduced contact
351 between the hair cells and the sensory axons in the *sema7a*$^{-/-}$ mutants or from the lack of
352 Sema7A-mediated juxtracrine signaling onto the apposed neurite terminals (15).

353 **Discussion**

354 The specification of neural circuitry requires precise control of the guidance cues that direct
355 and restrict neural arbors at their target fields and facilitate synapse formation. In the lateral-
356 line neuromast of the zebrafish, we have identified Sema7A as an essential cue that regulates
357 the interaction between hair cells and sensory axons. We have discovered dual modes of
358 Sema7A function *in vivo*: the chemoattractive diffusible form is sufficient to guide the sensory
359 arbors toward their target, whereas the membrane-attached form likely participates in sculping
360 accurate neural circuitry to facilitate contact-mediated formation and maintenance of synapses.
361 Our results suggest a potential mechanism for hair cell innervation in which a local Sema7A^{sec}
362 diffusive cue consolidates the sensory arbors at the hair cell cluster and the membrane-
363 anchored Sema7A-GPI molecule regulates microcircuit topology and synapse assembly.

364 The role of Sema7A in regulating diverse topological features of the arborization network
365 suggests that microcircuits of control and *sema7a*$^{-/-}$ neuromasts display important functional
366 differences. Loss of Sema7A disrupts the hierarchical organization of the node-degree
367 distribution along the organ's axis, as well as the preference towards forming loops containing
368 four nodes with 30-40 μm of arbors. What benefit does the network gain from surrounding the
369 hair cell cluster with closed loops instead of bare terminals? The network may actively form
370 loops to contribute to the neuromast's overall structure and function, or else emerge as a
371 consequence of the arbors navigating the intervening spaces between the hair cells and
372 support cells. Through our ectopic expression of Sema7A^{sec}, we have observed that free
373 spaces and physical obstructions can shape arbor morphologies, such as in the myotomal
374 niche. However, we speculate that the precise patterning of the network—with characteristic
375 looping behaviors—is not merely a byproduct of neuromast architecture, but rather contributes

376 to the network's ability to perform robust neural computations and faithfully transmit sensory
377 information to higher processing centers in the posterior lateral-line ganglion and medial
378 octavolateralis nucleus in the hindbrain (7). Further studies are necessary to dissect the
379 potential role of these topological features in performing robust neural computations in the
380 lateral-line microcircuit.

381 Recent studies have begun to dissect the molecular mechanisms of semaphorin
382 signaling in axonal navigation. In explants derived from the murine olfactory bulb, Sema7A
383 interacts directly with integrinβ1 to trigger downstream signaling effectors involving focal
384 adhesion kinase and mitogen-activated protein kinases, which are critical regulators of the
385 cytoskeletal network during axonal pathfinding (4,38). Moreover, the interaction between
386 Sema7A and its receptor plexinC1 activates the rac1-cdc42-PAK pathway, which alters the
387 actin network to promote axonal guidance and synapse formation (15,39). We speculate that
388 lateral-line sensory axons utilize similar mechanisms to sense and respond to Sema7A in the
389 establishment of microcircuits with hair cells.

390 During early development of the posterior lateral line, the growth cones of sensory axons
391 intimately associate with the prosensory primordium that deposits neuromasts along the lateral
392 surface of the larva (40,41). The growth of the sensory fibers with the primordium is regulated
393 by diverse neurotrophic factors expressed in the primordium (42,43). Impairing brain-derived
394 or glial cell line-derived neurotrophic factors and their receptors perturbs directed axonal
395 motility and innervation of hair cells (42,43). Lateral-line hair cells are particularly enriched in
396 brain-derived neurotrophic factor (44) and other chemotropic cues (Figure 6). Because the
397 sensory axons of *sema7a*$^{-/-}$ mutants reliably branch from the lateral-line nerve to reach hair cell
398 clusters, these chemoattractive factors might compensate in part for the absence of Sema7A
399 function. Although sensory axons are strict selectors of hair cell polarity and form synapses
400 accordingly (5), diverse chemoattractant cues including Sema7A occur uniformly between hair
401 cell polarities (44). It seems likely that unbiased attractive signals bring sensory arbors toward
402 hair cells, after which polarity-specific molecules on hair cell surfaces dictate the final
403 association between axonal terminal and hair cells. Notch-delta signaling and its downstream

404 effectors regulate hair cell polarity and the innervation pattern (6,8,25). It would be interesting
405 to determine whether Notch-mediated polarity signatures on the hair cell's surface can refine
406 the neuromast neural circuitry.

407 **Materials and Methods**

408 **Zebrafish strains and husband**ry. Experiments were performed on 1.5-4 dpf zebrafish larvae
409 in accordance with the standards of Rockefeller University's Institutional Animal Care and Use
410 Committee. Naturally spawned and fertilized eggs were collected, cleaned, staged, and
411 maintained at 28.5 ºC in system-water with 1 µg/mL methylene blue. Wild-type AB and
412 heterozygous mutant *semaphorin7a*^{sa24691} zebrafish were obtained from the Zebrafish
413 International Resource Center. In addition, the following transgenic zebrafish lines were used:
414 *Tg(myo6b:actb1-EGFP)* (45), *Tg(neurod1:tdTomato)* (25), and *TgBAC(neurod1:EGFP)* (46).

415 **Genotyping of mutant fish.** The *semaphorin7a*^{sa24691} allele harbors an A-to-T point mutation
416 in the seventh exon of the *semaphorin7a* gene, which creates a premature stop codon (Fig.
417 S2A). Genomic DNA was isolated from the tail fins of adult *semaphorin7a*^{sa24691} (*sema7a*^{sa91})
418 heterozygous mutant zebrafish. The mutant locus in the genome was PCR amplified using the
419 following primers: sema7a^{sa91}F: 5´-AAAGCTGGAAAGCGAATCAA-3´ and sema7a^{sa91}R:
420 5´-ATATCCAAGGATCCGCCTCT-3´. The 734-base pair amplicons were sequenced, and
421 heterozygous adults were propagated.

422 **Reverse transcription-polymerase chain reactions (RT PCR).** Total RNA was isolated from
423 whole zebrafish larvae by TRIzol extraction followed by DNAse treatment (TURBO DNA-free
424 Ambion). We used thirty 4 dpf zebrafish larvae to isolate total RNA. We generated cDNA
425 libraries using iScript cDNA Synthesis Kit (Bio-Rad). Each transcript was PCR amplified using
426 the following primers: sema7aF: 5´-GGTTTTTCTGAGGCCATTCC-3´, sema7aR1:
427 5´-GGCACTCGTGACAAATGCTA-3´, sema7aR2: 5´-TGTGGAGAAAGTCACAAAGCA-3´
428 (Fig. S1A).

429 **Transient transgenesis with the hsp70l:sema7a^{sec}-mKate2 construct.** The pDNR-LIB
430 plasmid containing the *sema7a^{sec}* coding sequence was purchased from horizon (7140389,
431 Perkin-Elmer). The coding sequence was PCR amplified using the following primers:
432 sema7a^{sec}F:
433 5´-GGGGACAAGTTTGTACAAAAAAGCAGGCTTGATGATTCGACATTATTCT-3´ and
434 sema7a^{sec}R:
435 5´-GGGGACCACTTTGTACAAGAAAGCTGGGTG*CTT*TGTGGAGAAAGTCACAAAGCA-3´.
436 The italicized nucleotides denote the mutated stop codon. The amplicon was then cloned into
437 the pDONR221 vector by BP recombination to generate the middle entry pME-sema7a^{sec}
438 vector. To generate the hsp70:sema7a^{sec}-mKate2 construct, gateway cloning was performed
439 by combining the plasmids p5E-hsp70 (47), pME-sema7a^{sec}, p3E-mKate2-myc no-pA
440 (Addgene, 80812), and pDESTtol2pACrymCherry (Addgene, 64023) with LR Clonase II Plus
441 (Invitrogen). Verified constructs (25 ng/µl plasmid DNA) were injected with Tol2 Transposase
442 mRNA (approximately 25 ng/µl) into one-cell embryos. The transiently transgenic larvae—
443 identified by the expression of red fluorescent protein (mCherry) in their lenses—were raised
444 till 3 dpf, heat-shocked in a water bath at 37 ºC for 1 hr, incubated at 28 ºC for 1 hr to allow
445 expression, and subsequently mounted for live imaging.

446 **Microscopy and volumetric rendering of living neuronal arbors and cells.** Living larvae
447 were dechorionated, anaesthetized in 600 µM 3-aminobenzoic acid ethyl ester
448 methanesulfonate in system-water with 1 µg/mL methylene blue, and mounted in 1 % low-
449 melting-point agarose on a glass-bottom MetTek dish at specific stages. The larvae were
450 maintained at 28 °C during imaging in a temperature-controlled stage top chamber (OKO Lab
451 UNO-T). Images at successive focal depths were captured at 200 nm intervals and
452 deconvolved with Microvolution software in ImageJ (NIH). The three-dimensional datasets
453 were processed and volume-rendered with the surface evolver and filament-tracer tools in
454 Imaris (Bitplane, Belfast, UK). The Imaris workstation was provided by the Rockefeller
455 University Bio-imaging Resource Center.

456 **Immunofluorescence microscopy.** For the immunofluorescence labeling of wholemounted
457 wild-type control and *sema7a*$^{-/-}$ larvae, 1.5-4 dpf larvae were fixed overnight at 4 °C in 4 %
458 formaldehyde in phosphate-buffered saline solution (PBS) with 1 % Tween-20 (1 % PBST).
459 Larvae were washed four times with 1 % PBST for 15 min each, then placed for 2 hr in blocking
460 solution containing PBS, 2 % normal donkey serum (NDS), 0.5 % Tween-20, and 1 % BSA.
461 Primary antibodies were diluted in fresh blocking solution and incubated with the specimens
462 overnight at 4 °C. The primary antibodies were goat anti-Sema7A (1:200; AF1835, R&D
463 Systems) (14), rabbit anti-myosin VI (1:200; Proteus 25-6791), murine anti-GM130 (1:200;
464 610822, BD Transduction Laboratories), murine anti-CTBP (1:200; B-3, SC-55502, Santa Cruz
465 Biotech), and rabbit anti-mCherry (1:200; GTX128508, GeneTex). Larvae were washed four
466 times with 0.1% PBST for 15 min each. Alexa Fluor-conjugated secondary antibodies
467 (Invitrogen, Molecular Probes) applied overnight at 1:200 dilutions in 0.2 % PBST included anti-
468 rabbit (488 nm), anti-goat (555 nm), and anti-mouse (647 nm). Larvae were then washed four
469 times in 0.2 % PBST for 15 min each and stored at 4 °C in VectaShield (Vector Laboratories).
470 For the immunofluorescence labeling of postsynaptic density in wholemounted wild-type
471 control and *sema7a*$^{-/-}$ larvae, 2-4 dpf larvae were fixed with 4 % formaldehyde in PBS for
472 4.5-6 hr at 4 °C. Larvae were washed five times with 0.01 % PBST for 5 min each and then
473 rinsed in distilled water for 5 min. The larvae were permeabilized with ice-cold acetone at -20 °C
474 for 5 min. They were rinsed in distilled water for 5 min, washed five times with 0.01 % PBST
475 for 5 min each, and blocked overnight with PBS buffer containing 2 % goat serum and 1 %
476 BSA. Murine anti-pan-MAGUK antibody (1:500; IgG1 NeuroMab, K28.86, 75-029) was diluted
477 in PBS containing 1 % BSA, added to the larvae, and incubated for 3 hr at room temperature.
478 Larvae were washed five times for 5 min each with 0.01 % PBST. Alexa Fluor 555-conjugated
479 anti-mouse secondary antibody (1:1000) diluted in PBS containing 1 % BSA was added to the
480 larvae and incubated for 2 hr at room temperature. Larvae were washed five times with 0.01 %
481 PBST for 5 min each, rinsed in distilled water for 5 min, and stored at 4 °C in VectaShield
482 (Vector Laboratories).

483 Posterior segments of fixed larvae were mounted on a glass slide and imaged with a
484 microlens-based, super-resolution confocal microscope (VT-iSIM, VisiTech international)
485 under 60X and 100X, silicone-oil objective lenses of numerical apertures 1.30 and 1.35,
486 respectively. Images at successive focal depths were captured at 200 nm intervals and
487 deconvolved with the Microvolution software in ImageJ.

488 **Measurement of Sema7A intensity.** The average Sema7A fluorescence intensities of the hair
489 cells from 1.5 dpf, 2 dpf, 3 dpf, and 4 dpf neuromasts were measured by determining the mean
490 gray level within each hair cell labeled by actin-GFP expression. The intensity distribution of
491 Sema7A protein along the apicobasal axis of the hair cell was measured using the line profile
492 tool in ImageJ (Figure 1—figure supplement 1F). Because hair cell lengths differed among
493 samples, lines were drawn with 2 µm widths and varying lengths of 6-8 µm. For each hair cell,
494 apicobasal length was scaled from 0 to 100 arbitrary units and the intensity values from 0 to 1
495 arbitrary units.

496 **Generation of skeletonized networks.** The labeled sensory axons were traced in three
497 dimensions with ImageJ's semi-automated framework, SNT (48). Each trace depicts the
498 skeletonized form of the posterior lateral-line nerve, the posterior lateral-line branch, and the
499 point of arborization from which the sensory arbors radiate to contact the hair cells (Fig. 2D,E).
500 The three-dimensional pixels or voxels obtained from the skeletonized sensory arbor traces
501 were processed using custom code written in Python for visual representation and quantitative
502 analysis.

503 **Generation of combined hair cell clusters and the corresponding combined skeletonized**
504 **networks.** The hair cell clusters of neuromasts from each developmental stage were aligned
505 by the centers of their apices, which were identified by the hair bundles, and overlayed to
506 generate combined hair cell clusters using custom Python code. The associated skeletonized
507 sensory-arbor traces at each developmental stage were aligned similarly using custom Python
508 code. The details of the procedures are available upon request and the corresponding code is
509 available on GitHub.

Quantification of sensory arbor distributions around hair cell clusters. The region from the center of the combined hair cell cluster to 60 µm in the post-cluster region was divided into 3600 concentric sections of equal area (Figure 2—figure supplement 2A). Each section, as depicted with a distinct color shade, had an area of π µm^2. Sensory arbor density was defined as Log_{10}[(Area occupied by the arbors in each section)/ (Area of each section)]. The arbor density was then plotted as a histogram against distance from the center of the combined hair cell cluster. Each bin of the histogram represents an area of π μm^2. The histograms were finally represented as density trace graphs with Kernel Density Estimation (KDE) in Python.

Quantification of contact between sensory arbors and hair cell clusters. For each hair cell cluster, the voxels of the sensory arbor traces that were inside or within 0.5 μm—the average neurite radius—of the cluster boundary were denoted as arbors in contact with their corresponding hair cell cluster (Figure 2—figure supplement 2B). The percentage of arbors in contact with each hair cell cluster was defined as: (Number of voxels that remained inside the cluster boundary/Total number of voxels in the arbor) X 100. The data were analyzed through an automated pipeline with custom code.

Quantification of the sensory arborization network topology. We developed a custom Python script (snt_topology.py; available on GitHub) to convert the skeletonized sensory arborization networks to network graphs (NetworkX, v3.1). We first used a custom ImageJ macro to convert SNT skeletons to csv files, then generated the network graph from the individual arbor paths. As noted previously, we defined five topological attributes: (1) nodes—junctions where arbors branch, converge, or cross; (2) loops—minimal arbor cycles forming topological holes; (3) bare terminals—arbors with free ends; (4) node degree—the number of first-neighbor nodes incident to a node; and (5) arbor curvature—the total curvature of a bare terminal (Figure 3A). To enumerate loops and quantify their lengths and node numbers, we computed the minimum cycle basis for each network graph. The relative organ height of each node in a graph was defined in 3D using Equation (1):

$$(\vec{u} \cdot \vec{v}) \,/\, \|\vec{v}\|^2 , \qquad (1)$$

537 where $\vec{u}$ is the vector from the arborization initiation point to a node and $\vec{v}$ is the vector from the
538 arborization initiation point to the hair cell cluster apex. The relative occurrence of nodes (Figure
539 3—figure supplement 1A-C) was normalized by both the number of hair cells per neuromast
540 and the total number of neuromasts, for comparison across ages and genotypes. The relative
541 number of bare terminals and loops (Figure 3B; Figure 3—figure supplement 1D, E) was
542 normalized by the number of hair cells per neuromast and scaled between 0 and 1. The density
543 was then normalized by the total number of neuromasts imaged for each developmental stage
544 and genotype. For Figure 3C and Figure 3—figure supplement 1F and G, the normalized
545 occurrence was computed as the number of arbors of a given length that formed either a bare
546 terminal or a loop, divided by the total number of arbors of either feature of that length. Lastly,
547 we defined bare terminals as having either high or low curvature (Figure 3F; Figure 3—figure
548 supplement 2C, D) if their absolute total signed curvature [Equation (2)] in three dimensions
549 was either higher or lower than $\pi/6$, respectively:

550 $$\left| \int \frac{dT}{ds} \cdot N(s)\, ds \right|, \qquad (2)$$

551 where s is the arc-length parameter of the bare terminal, $T(s)$ is the unit tangent vector at each
552 point along the arbor, $N(s)$ is the unit normal vector at each point, and the integral is evaluated
553 from the terminal's branching node to the arbor's tip. For a closed curve forming a full loop, this
554 value will equal 2π. In practice, we first fit B-splines (scipy.interpolate.splprep; SciPy, v1.10.1)
555 in 3D to the skeletons for each bare terminal before evaluating their derivatives
556 (scipy.interpolate.splev) and integrating (scipy.integrate.simpson) over their lengths.

557 **Quantification of aberrant sensory arborization in ectopic Sema7A^{sec} expression.** The
558 sensory arbor networks were traced in three dimensions with SNT. The surface of each of the
559 ectopically expressing Sema7A^{sec}-mKate2 cells was represented by a single point that was
560 closest to the terminal point of the guided neurite. Distances between two points were
561 calculated using standard mathematical operations.

Statistical analysis. Data visualization and statistical analysis were conducted with GraphPad Prism (Version 9) and Python (v3.10). The Mann-Whitney test was used for hypothesis testing unless otherwise noted, and the statistical details are given in the respective figure legends.

Data and code availability. Owing to size restrictions, the experimental image data have not been uploaded to a repository but are available from the corresponding author on request. The code generated during this study is available on GitHub (https://github.com/agnikdasgupta/Sema7A_regulates_neural_circuitry).

Acknowledgments. The authors thank Nicolas Velez and Emily Atlas for valuable discussions. Samantha Campbell and Anna Kaczynska provided expert fish husbandry. Katie Kindt kindly provided various strains of zebrafish. Image processing benefitted from facilities at the Bio-Imaging Resource Center. A.D. was supported by a Kavli Neural Systems Institute Postdoctoral Fellowship from The Rockefeller University. C.C.R. is supported by National Science Foundation Graduate Research Fellowship Grant No. 1946429. A.J., S.P.P., and L.M.S. were supported by Howard Hughes Medical Institute, of which A.J.H. is an Investigator.

Author Contributions

A.D. initiated the project, conducted experiments, analyzed data, and quantified results. C.C.R developed the Python codes for the network topology analysis and quantified those results, as well as analyzed published transcriptomics data. S.P.P. developed the Python codes for three-dimensional visual representation of sensory arbors and quantified arbor morphologies. L.M.S. conducted preliminary experiments. A.J. plotted Sema7A intensity measurements. A.D. wrote the paper with contributions from C.C.R and A.J.H.

Declaration of Interests

The authors declare no competing interests.

585 **References**

586 1. Lykissas M, Batistatou A, Charalabopoulos K, Beris A. The Role of Neurotrophins in
587 Axonal Growth, Guidance, and Regeneration. Curr Neurovasc Res. 2007 May 1;4(2):143–
588 51.

589 2. Vaccaro G, Dumoulin A, Zuñiga NR, Bandtlow CE, Stoeckli ET. The Nogo-66 Receptors
590 NgR1 and NgR3 Are Required for Commissural Axon Pathfinding. J Neurosci. 2022 May
591 18;42(20):4087–100.

592 3. Nguyen-Ba-Charvet KT, Di Meglio T, Fouquet C, Chedotal A. Robos and Slits Control the
593 Pathfinding and Targeting of Mouse Olfactory Sensory Axons. J Neurosci. 2008 Apr
594 16;28(16):4244–9.

595 4. Jeroen Pasterkamp R, Peschon JJ, Spriggs MK, Kolodkin AL. Semaphorin 7A promotes
596 axon outgrowth through integrins and MAPKs. Nature. 2003 Jul;424(6947):398–405.

597 5. Nagiel A, Andor-Ardo D, Hudspeth AJ. Specificity of Afferent Synapses onto Plane-
598 Polarized Hair Cells in the Posterior Lateral Line of the Zebrafish. J Neurosci. 2008 Aug
599 20;28(34):8442–53.

600 6. Jacobo A, Dasgupta A, Erzberger A, Siletti K, Hudspeth AJ. Notch-Mediated Determination
601 of Hair-Bundle Polarity in Mechanosensory Hair Cells of the Zebrafish Lateral Line. Curr
602 Biol. 2019 Nov;29(21):3579-3587.e7.

603 7. Valera G, Markov DA, Bijari K, Randlett O, Asgharsharghi A, Baudoin JP, et al. A neuronal
604 blueprint for directional mechanosensation in larval zebrafish. Curr Biol. 2021
605 Apr;31(7):1463-1475.e6.

606 8. Dow E, Jacobo A, Hossain S, Siletti K, Hudspeth AJ. Connectomics of the zebrafish's
607 lateral-line neuromast reveals wiring and miswiring in a simple microcircuit. eLife. 2018 Jun
608 12;7:e33988.

609 9. Lush ME, Diaz DC, Koenecke N, Baek S, Boldt H, St Peter MK, et al. scRNA-Seq reveals
610 distinct stem cell populations that drive hair cell regeneration after loss of Fgf and Notch
611 signaling. eLife. 2019 Jan 25;8:e44431.

612 10. Carulli D, de Winter F, Verhaagen J. Semaphorins in Adult Nervous System Plasticity
613 and Disease. Front Synaptic Neurosci. 2021 May 11;13:672891.

614 11. Yazdani U, Terman JR. The semaphorins. Genome Biol. 2006;7(3):211.

615 12. de Winter F, Kwok JCF, Fawcett JW, Vo TT, Carulli D, Verhaagen J. The
616 Chemorepulsive Protein Semaphorin 3A and Perineuronal Net-Mediated Plasticity. Neural
617 Plast. 2016;2016:1–14.

618 13. Coate TM, Spita NA, Zhang KD, Isgrig KT, Kelley MW. Neuropilin-2/Semaphorin-3F-
619 mediated repulsion promotes inner hair cell innervation by spiral ganglion neurons. eLife.
620 2015 Aug 24;4:e07830.

621 14. Carcea I, Patil SB, Robison AJ, Mesias R, Huntsman MM, Froemke RC, et al.
622 Maturation of cortical circuits requires Semaphorin 7A. Proc Natl Acad Sci. 2014 Sep
623 23;111(38):13978–83.

624 15. Inoue N, Nishizumi H, Naritsuka H, Kiyonari H, Sakano H. Sema7A/PlxnCl signaling
625 triggers activity-dependent olfactory synapse formation. Nat Commun. 2018
626 Dec;9(1):1842.

627 16. Inoue N, Nishizumi H, Ooyama R, Mogi K, Nishimori K, Kikusui T, et al. The olfactory
628 critical period is determined by activity-dependent Sema7A/PlxnC1 signaling within
629 glomeruli. eLife. 2021 Mar 29;10:e65078.

630 17. Morote-Garcia JC, Napiwotzky D, Köhler D, Rosenberger P. Endothelial Semaphorin
631 7A promotes neutrophil migration during hypoxia. Proc Natl Acad Sci. 2012 Aug
632 28;109(35):14146–51.

633 18. Nishide M, Kumanogoh A. The role of semaphorins in immune responses and
634 autoimmune rheumatic diseases. Nat Rev Rheumatol. 2018 Jan;14(1):19–31.

635 19. Köhler D, Granja T, Volz J, Koeppen M, Langer HF, Hansmann G, et al. Red blood
636 cell-derived semaphorin 7A promotes thrombo-inflammation in myocardial ischemia-
637 reperfusion injury through platelet GPIb. Nat Commun. 2020 Dec;11(1):1315.

638 20. Pham TL, He J, Kakazu AH, Jun B, Bazan NG, Bazan HEP. Defining a mechanistic
639 link between pigment epithelium–derived factor, docosahexaenoic acid, and corneal nerve
640 regeneration. J Biol Chem. 2017 Nov;292(45):18486–99.

641 21. Xie J, Wang H. Semaphorin 7A as a potential immune regulator and promising
642 therapeutic target in rheumatoid arthritis. Arthritis Res Ther. 2017 Dec;19(1):10.

643 22. Dow E, Siletti K, Hudspeth AJ. Cellular projections from sensory hair cells form
644 polarity-specific scaffolds during synaptogenesis. Genes Dev. 2015 May 15;29(10):1087–
645 94.

646 23. Pujol-Martí J, Faucherre A, Aziz-Bose R, Asgharsharghi A, Colombelli J, Trapani JG,
647 et al. Converging Axons Collectively Initiate and Maintain Synaptic Selectivity in a
648 Constantly Remodeling Sensory Organ. Curr Biol. 2014 Dec;24(24):2968–74.

649 24. De Wit J, De Winter F, Klooster J, Verhaagen J. Semaphorin 3A displays a punctate
650 distribution on the surface of neuronal cells and interacts with proteoglycans in the
651 extracellular matrix. Mol Cell Neurosci. 2005 May;29(1):40–55.

652 25. Ji YR, Warrier S, Jiang T, Wu DK, Kindt KS. Directional selectivity of afferent neurons
653 in zebrafish neuromasts is regulated by Emx2 in presynaptic hair cells. eLife. 2018 Apr
654 19;7:e35796.

655 26. Diaz-Horta O, Abad C, Sennaroglu L, Foster J, DeSmidt A, Bademci G, et al. ROR1 is
656 essential for proper innervation of auditory hair cells and hearing in humans and mice. Proc
657 Natl Acad Sci U S A. 2016 May 24;113(21):5993–8.

658 27. Newman M. The structure of real-world networks [Internet]. Vol. 1. Oxford University
659 Press; 2018 [cited 2023 May 2]. Available from:
660 https://academic.oup.com/book/27884/chapter/203817512

661 28. Sharma P, Ruel TD, Kocha KM, Liao S, Huang P. Single cell dynamics of embryonic
662 muscle progenitor cells in zebrafish. Development. 2019 Jan 1;dev.178400.

663 29. Keenan SR, Currie PD. The Developmental Phases of Zebrafish Myogenesis. J Dev
664 Biol. 2019 Jun 2;7(2):12.

665 30. Sato A, Koshida S, Takeda H. Single-cell analysis of somatotopic map formation in the
666 zebrafish lateral line system. Dev Dyn. 2010 Jul;239(7):2058–65.

667 31. Shen K, Cowan CW. Guidance Molecules in Synapse Formation and Plasticity. Cold
668 Spring Harb Perspect Biol. 2010 Apr 1;2(4):a001842–a001842.

669 32. Um JW, Ko J. Neural Glycosylphosphatidylinositol-Anchored Proteins in Synaptic
670 Specification. Trends Cell Biol. 2017 Dec;27(12):931–45.

671 33. Uesaka N, Uchigashima M, Mikuni T, Nakazawa T, Nakao H, Hirai H, et al. Retrograde
672 semaphorin signaling regulates synapse elimination in the developing mouse brain.
673 Science. 2014 May 30;344(6187):1020–3.

674 34. Sheets L, Hagen MW, Nicolson T. Characterization of Ribeye Subunits in Zebrafish
675 Hair Cells Reveals That Exogenous Ribeye B-Domain and CtBP1 Localize to the Basal
676 Ends of Synaptic Ribbons. Riley B, editor. PLoS ONE. 2014 Sep 10;9(9):e107256.

677 35. Oliva C, Escobedo P, Astorga C, Molina C, Sierralta J. Role of the maguk protein
678 family in synapse formation and function. Dev Neurobiol. 2012 Jan;72(1):57–72.

679 36. Suli A, Pujol R, Cunningham DE, Hailey DW, Prendergast A, Rubel EW, et al.
680 Innervation regulates synaptic ribbons in lateral line mechanosensory hair cells. J Cell Sci.
681 2016 Jan 1;jcs.182592.

682 37. Taschenberger H, Leão RM, Rowland KC, Spirou GA, von Gersdorff H. Optimizing
683 Synaptic Architecture and Efficiency for High-Frequency Transmission. Neuron. 2002
684 Dec;36(6):1127–43.

685 38. Myers JP, Gomez TM. Focal Adhesion Kinase Promotes Integrin Adhesion Dynamics
686 Necessary for Chemotropic Turning of Nerve Growth Cones. J Neurosci. 2011 Sep
687 21;31(38):13585–95.

688 39. O'Donnell M, Chance RK, Bashaw GJ. Axon Growth and Guidance: Receptor
689 Regulation and Signal Transduction. Annu Rev Neurosci. 2009 Jun 1;32(1):383–412.

690 40. Gilmour D, Knaut H, Maischein HM, Nüsslein-Volhard C. Towing of sensory axons by
691 their migrating target cells in vivo. Nat Neurosci. 2004 May;7(5):491–2.

692 41. Metcalfe WK. Sensory neuron growth cones comigrate with posterior lateral line
693 primordial cells in zebrafish. J Comp Neurol. 1985 Aug 8;238(2):218–24.

694 42. Gasanov EV, Rafieva LM, Korzh VP. BDNF-TrkB Axis Regulates Migration of the
695 Lateral Line Primordium and Modulates the Maintenance of Mechanoreceptor Progenitors.
696 Proost P, editor. PLOS ONE. 2015 Mar 9;10(3):e0119711.

697 43. Schuster K, Dambly-Chaudière C, Ghysen A. Glial cell line-derived neurotrophic factor
698 defines the path of developing and regenerating axons in the lateral line system of
699 zebrafish. Proc Natl Acad Sci. 2010 Nov 9;107(45):19531–6.

700 44. Germanà A, Laurà R, Montalbano G, Guerrera MC, Amato V, Zichichi R, et al.
701 Expression of Brain-Derived Neurotrophic Factor and TrkB in the Lateral Line System of
702 Zebrafish During Development. Cell Mol Neurobiol. 2010 Jul;30(5):787–93.

703 45. Kindt KS, Finch G, Nicolson T. Kinocilia Mediate Mechanosensitivity in Developing
704 Zebrafish Hair Cells. Dev Cell. 2012 Aug;23(2):329–41.

705 46. Obholzer N, Wolfson S, Trapani JG, Mo W, Nechiporuk A, Busch-Nentwich E, et al.
706 Vesicular Glutamate Transporter 3 Is Required for Synaptic Transmission in Zebrafish Hair
707 Cells. J Neurosci. 2008 Feb 27;28(9):2110–8.

708 47. Kwan KM, Fujimoto E, Grabher C, Mangum BD, Hardy ME, Campbell DS, et al. The
709 Tol2kit: A multisite gateway-based construction kit forTol2 transposon transgenesis
710 constructs. Dev Dyn. 2007 Nov;236(11):3088–99.

711 48. Arshadi C, Günther U, Eddison M, Harrington KIS, Ferreira TA. SNT: a unifying
712 toolbox for quantification of neuronal anatomy. Nat Methods. 2021 Apr;18(4):374–7.

713

714 **Figures and Figure Legends**

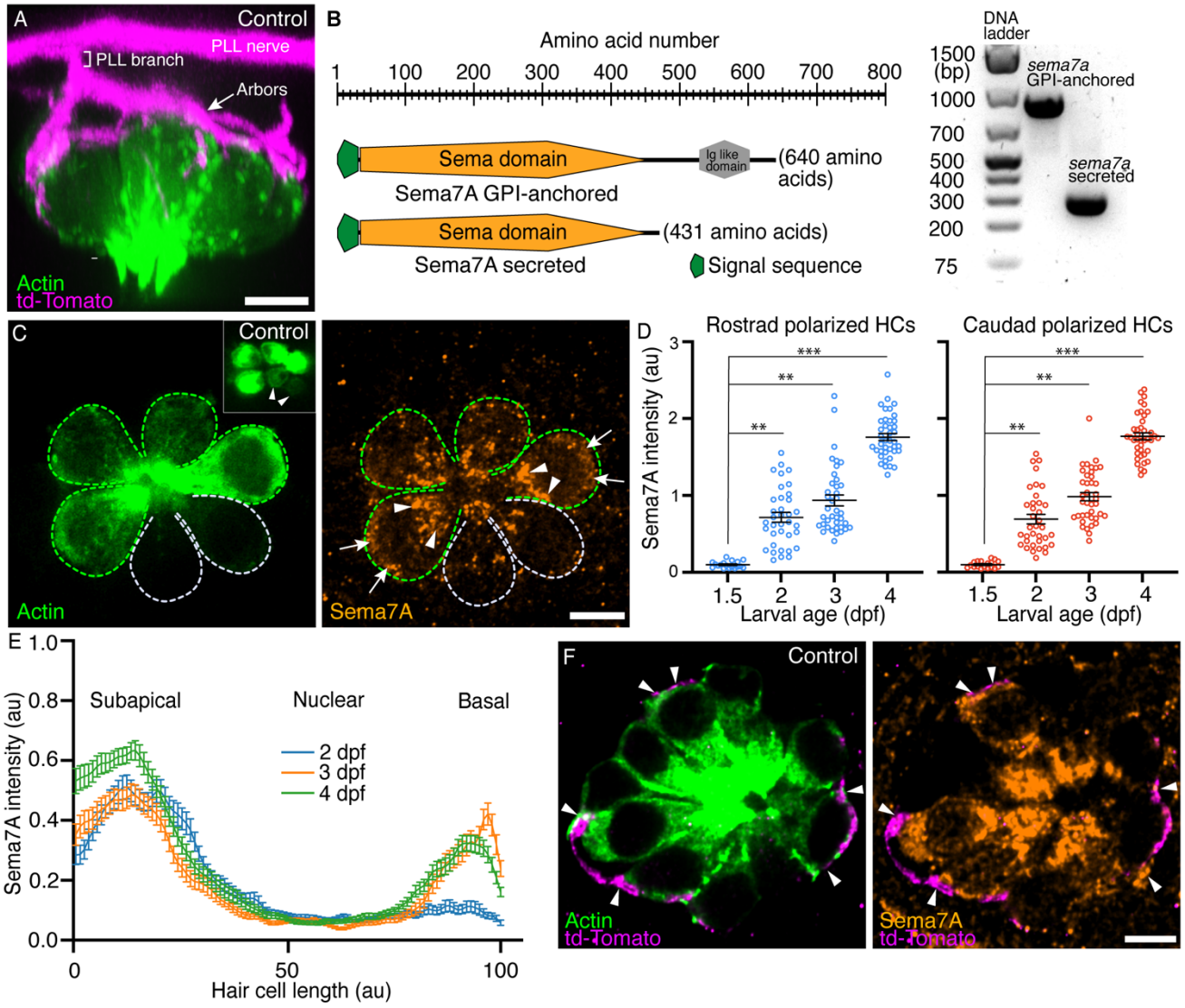

715 **Figure 1. Expression of Semaphorin7A in the zebrafish's lateral line.** (A) A volumetric
716 rendering of a PLL neuromast depicts the sensory axons (magenta) that branch from the lateral
717 line nerve to arborize around the basolateral surface of the hair cell cluster (green). Additional
718 cell types in the neuromast are not labeled. Larval age, 3 dpf. (B) A schematic drawing of the
719 two variants of the Sema7A protein molecule depicts the full-length GPI-anchored form and the
720 smaller, potentially secreted form. Both the molecules include a signal sequence (green) and
721 a conserved sema domain (orange). Gel-based RT-PCR analysis indicates the presence of
722 both the variants in developing larva. (C) A surface micrograph of a neuromast at 3 dpf depicts

723 two pairs of mature hair cells (green dashed lines) and a pair of immature hair cells (grey
724 dashed lines). Inset: among the three pairs of hair cell apices, the immature pair is indicated
725 by arrowheads. Immunolabeling reveals that the Sema7A protein (orange) occurs consistently
726 at the subapical region (arrowheads) and at the basolateral surface (arrows) of a hair cell. In
727 this and in each of the subsequent neuromast images, anterior is to the left and dorsal to the
728 top. (D) A plot quantifies developmental changes in the average Sema7A intensity in both
729 rostrally and caudally polarized hair cells of neuromasts from 1.5 dpf to 4 dpf. The data stem
730 from 18, 36, 39, and 40 hair cells in neuromasts of respectively 1.5 dpf, 2 dpf, 3 dpf, and 4 dpf
731 larvae. (E) A plot quantifies the distribution of average Sema7A intensity along the hair cell's
732 apicobasal axis. The results stem from 52, 57, and 54 hair cells of neuromasts from 2 dpf,
733 3 dpf, and 4 dpf larvae. (F) An immunofluorescence image at the nuclear level of a 4 dpf
734 neuromast shows the contact of the sensory arbors (magenta) with the basolateral surface of
735 the hair cells (green). Immunolabeling for Sema7A (orange) reveals enrichment of the protein
736 at the hair cell bases and sensory-axon interfaces (arrowheads). HC, hair cell; Scale bars,
737 5 μm; au, arbitrary unit; means ± SEMs; *** implies $p < 0.001$.

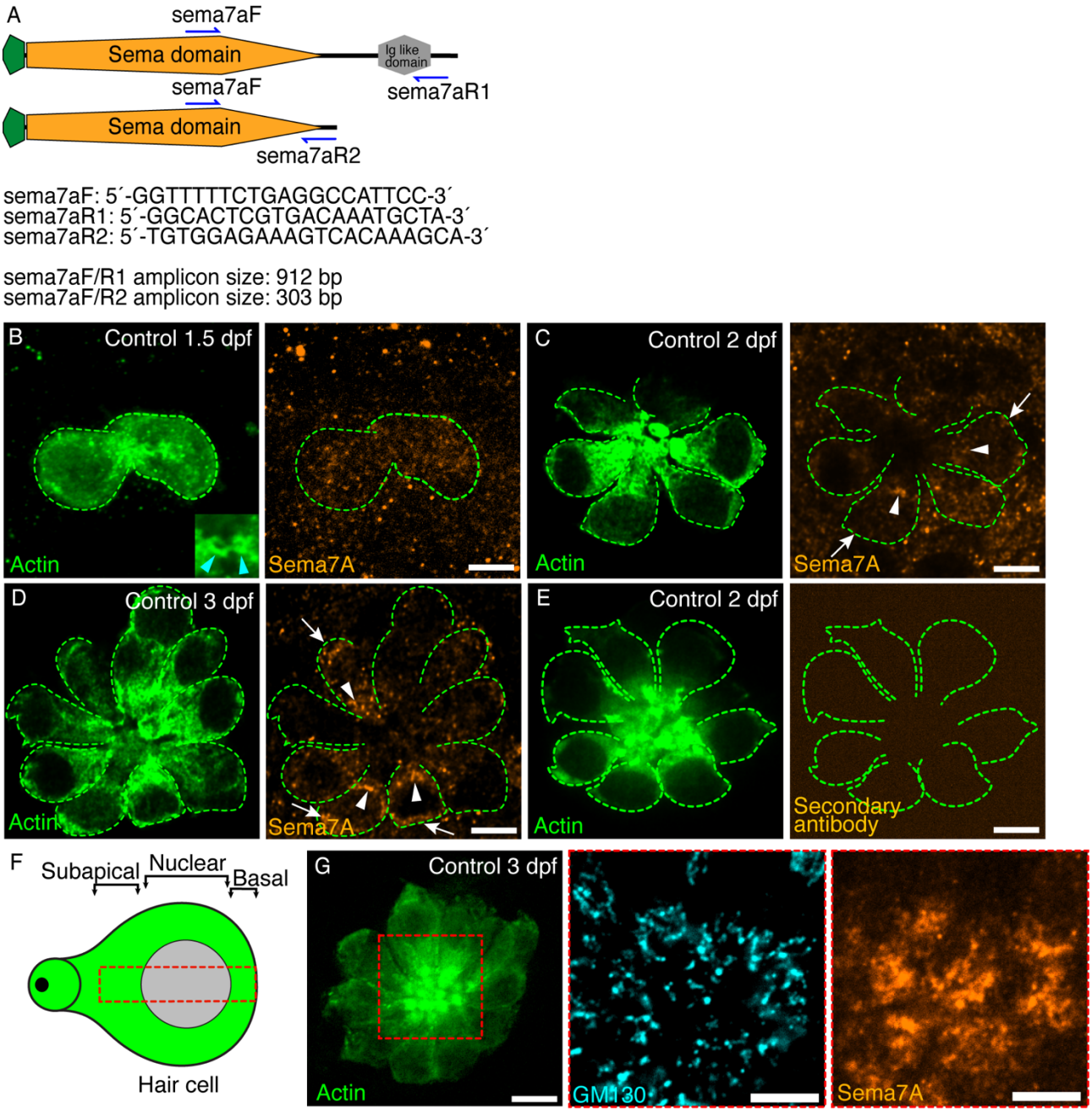

Figure 1—figure supplement 1. Expression of Semaphorin7A in the lateral line neuromast. (A) Distinct sets of primers (arrows) identify the two variants of the Sema7A protein molecule. (B-D) Surface micrographs show hair cells marked with actin-GFP (green dashed lines) and the localization of Sema7A protein (orange) in the subapical (arrowheads) and basal regions (arrows) of the corresponding hair cells from neuromasts of developing control larvae.

743 The inset in panel B depicts the apices of the immature hair cell pair. (E) Immunolabeling with
744 only the secondary antibody fails to detect any Sema7A signal. (F) A schematic diagram of a
745 single hair cell depicts the three distinct regions along the apicobasal axis of the cell. Sema7A
746 intensity was measured along this apicobasal axis (red dashed line). (G). A surface micrograph
747 depicts hair cells (green, left) whose subapical region (red dashed line) harbors the Golgi
748 network (cyan, middle) where the Sema7A protein is enriched (orange, right). Scale bars, 5 μm.

749 **Video 1. Sema7A is enriched at the hair cell base and sensory-axon interface**. A through-
750 focus scan of a 4 dpf control neuromast depicts the hair cells (green) that are innervated by the
751 sensory axons (magenta) at their basolateral surfaces where the Sema7A protein (orange) is
752 highly enriched. Scale bar, 5 μm.

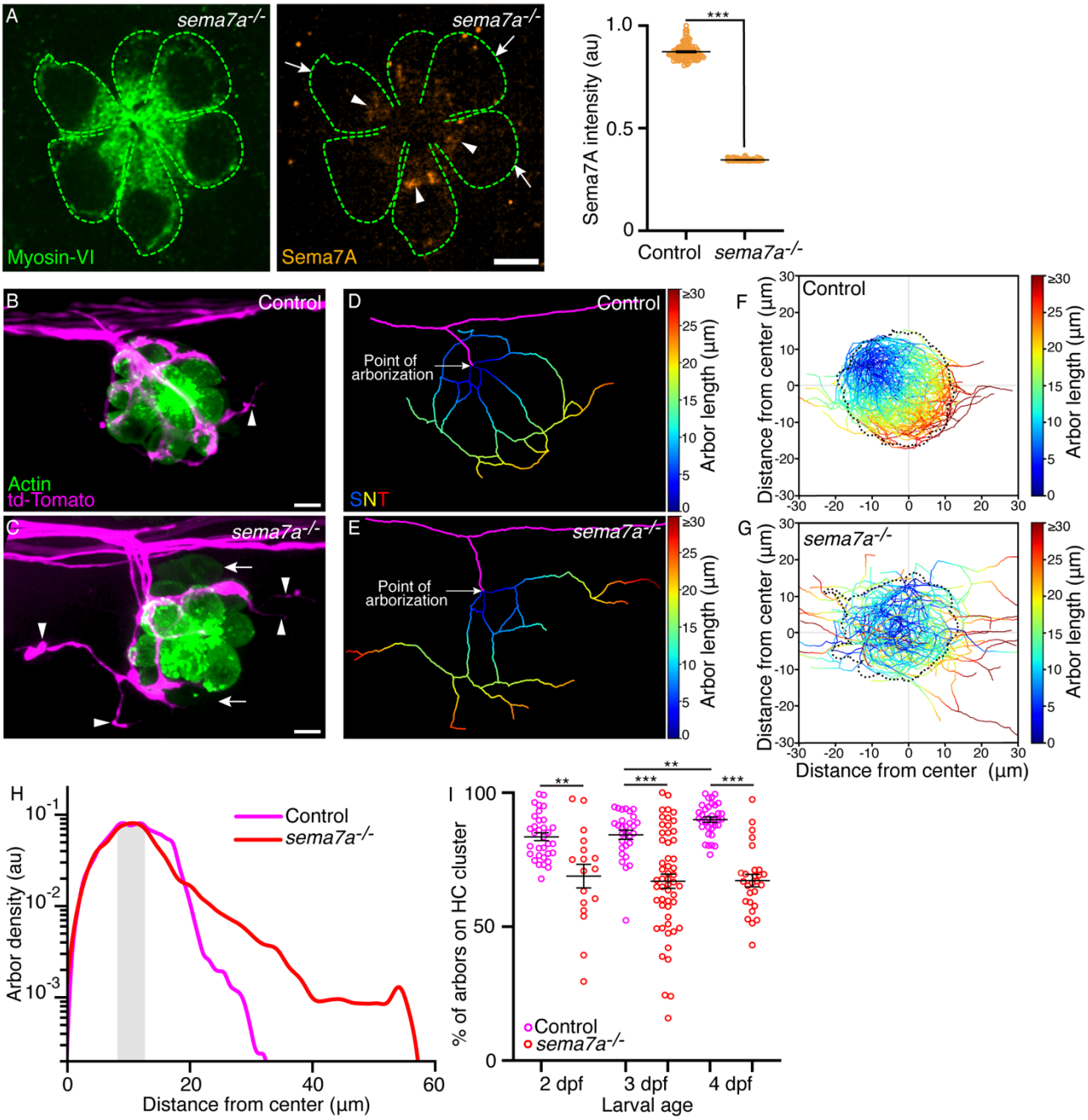

Figure 2. *sema7a*$^{-/-}$ mutants display aberrant sensory axon arborizations. (A) In a micrograph of a 3 dpf *sema7a*$^{-/-}$ neuromast, Myosin VI (green) marks the hair cells (green dashed lines) in which the level of Sema7A (orange) is highly reduced, with sporadic localization in the subapical region (arrowheads) and none in the basolateral (arrow) region. A plot of normalized Sema7A intensity from 99 control and 100 *sema7a*$^{-/-}$ hair cells quantitates the effect. (B,C) Surface views of a control and a *sema7a*$^{-/-}$ neuromast at 4 dpf depict the

759 interaction of the sensory arbors (magenta) with hair cell clusters (green). In the control, the
760 arbors intimately contact the hair cells, with a few exceptions (arrowhead). In the *sema7a*$^{-/-}$
761 mutant, the arbors direct many aberrant projections (arrowheads) away from the hair cell
762 cluster. The two immature hair cell pairs in the *sema7a*$^{-/-}$ neuromast are indicated by arrows.
763 (D,E) Skeletonized networks portray the three-dimensional topology of the sensory arbors from
764 the control and the *sema7a*$^{-/-}$ neuromasts depicted in panels B and C. The pseudocolored
765 trajectories depict the increase in arbor contour length from each point of arborization, defined
766 as the point at which the lateral line branch (magenta) contacts hair cell cluster.
767 (F,G) Micrographs depict the skeletonized networks of the combined 4 dpf hair cell clusters,
768 whose centers are located at (0,0). The X- and Y-coordinates represent the anteroposterior
769 (AP) and the dorsoventral (DV) axes of the larva, respectively. Positive values of the X- and
770 Y-coordinates represent the posterior and ventral directions, respectively. Combined
771 skeletonized network traces from 27 control and 27 *sema7a*$^{-/-}$ mutant neuromasts are
772 represented. H) The plot denotes the densities of the sensory arbors around the center of the
773 combined hair cell clusters for 35 control (magenta) and 27 *sema7a*$^{-/-}$ (red) neuromasts at 4 dpf.
774 The shaded area marks the region proximal to the boundary of the combined hair cell cluster.
775 (I) The plot quantifies the degree of contact of the sensory arbors to their hair cell clusters in
776 individual neuromasts from both control (magenta) and *sema7a*$^{-/-}$ mutants (red), each point
777 represents a single neuromast. Thirty-three, 29, and 35 neuromasts were analyzed from 2 dpf,
778 3 dpf, and 4 dpf control larvae, respectively. Seventeen, 53, and 27 neuromasts were analyzed
779 from 2 dpf, 3 dpf, and 4 dpf *sema7a*$^{-/-}$ mutant larvae, respectively. HC, hair cell; Scale bars,
780 5 μm; au, arbitrary unit; means ± SEMs; *** signifies $p < 0.001$; ** signifies $p < 0.01$.

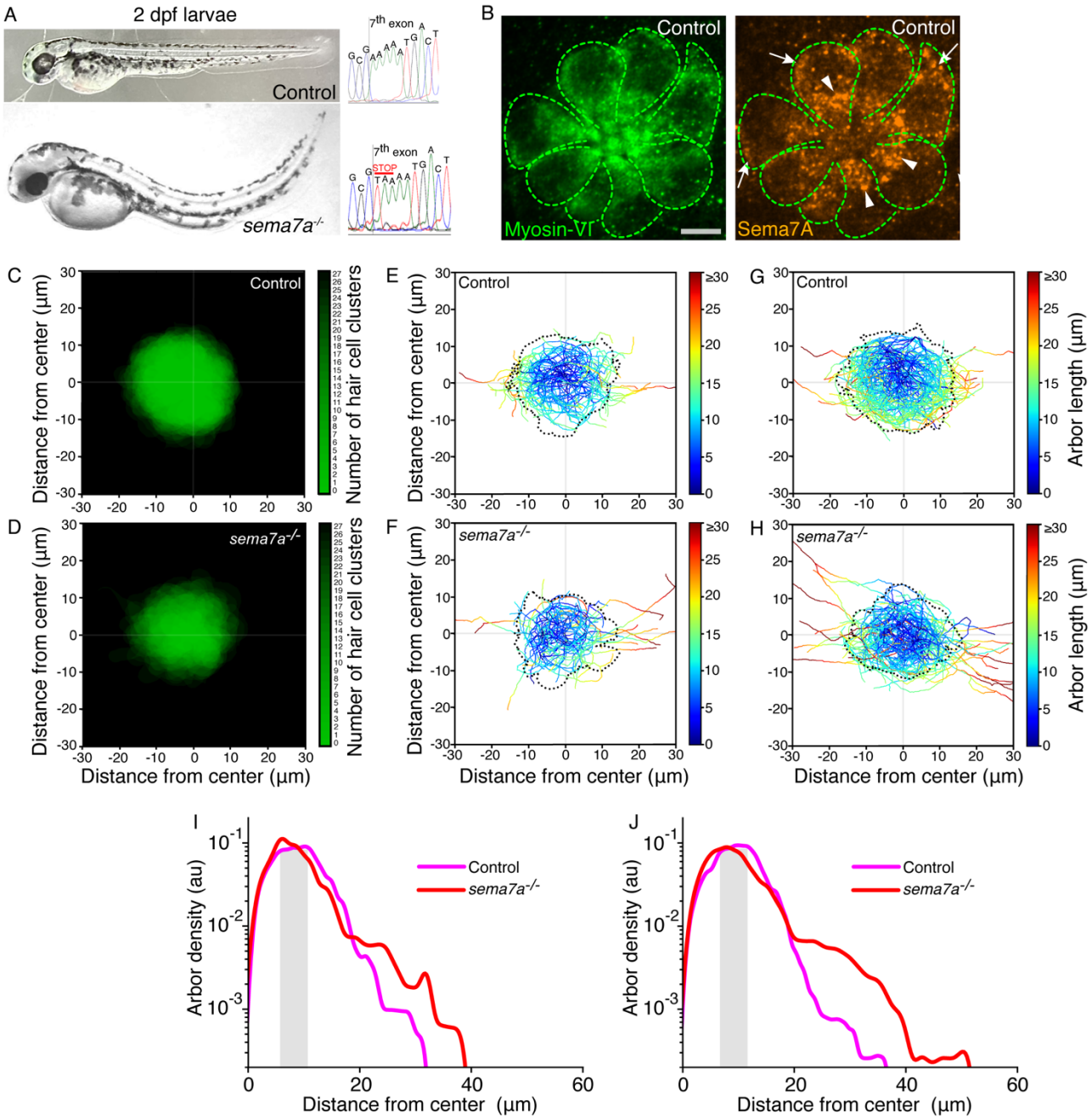

781 **Figure 2—figure supplement 1. *sema7a*$^{-/-}$ mutants exhibit aberrant sensory-axon**
782 **arborization throughout development.** (A) Micrographs depict the overall morphologies and
783 *sema7a* genomic profiles of 2 dpf control (top) and *sema7a*$^{-/-}$ larvae (bottom). (B) In a surface
784 micrograph of a 3 dpf control neuromast, myosin VI (green) marks hair cells (green dashed
785 lines). Sema7A (orange) protein is highly enriched in the subapical region (arrowheads) and
786 basolateral (arrow) region of the hair cells. (C,D) Micrographs depict combined 4 dpf hair cell
787 clusters, each of whose centers arise located at (0,0). The X- and Y-coordinates represent the

788 anteroposterior (AP) and dorsoventral (DV) axes of the larva, respectively. Positive values of
789 the X- and Y-coordinates represent posterior and ventral directions, respectively. Combined
790 hair cell clusters from 27 control and 27 *sema7a*$^{-/-}$ mutant neuromasts are represented.
791 (E,F) Micrographs depict the skeletonized networks of the combined 2 dpf hair cell clusters
792 from 17 control and 17 *sema7a*$^{-/-}$ mutant neuromasts. (G,H) Micrographs depict the
793 skeletonized networks of the combined 3 dpf hair cell clusters from 29 control and 29
794 *sema7a*$^{-/-}$ mutant neuromasts. (I) A plot quantitates the densities of the sensory arbors around
795 the center of the combined hair cell clusters for 33 control (magenta) and 17 *sema7a*$^{-/-}$ (red)
796 neuromasts at 2 dpf. The shaded area marks the region proximal to the boundary of the
797 combined hair cell cluster. (J) A plot quantitates the densities of the sensory arbors around the
798 center of the combined hair cell clusters for 29 control (magenta) and 53 *sema7a*$^{-/-}$ (red)
799 neuromasts at 3 dpf. The shaded area marks the region proximal to the boundary of the
800 combined hair cell cluster. Scale bar, 5 μm; au, arbitrary units.
801

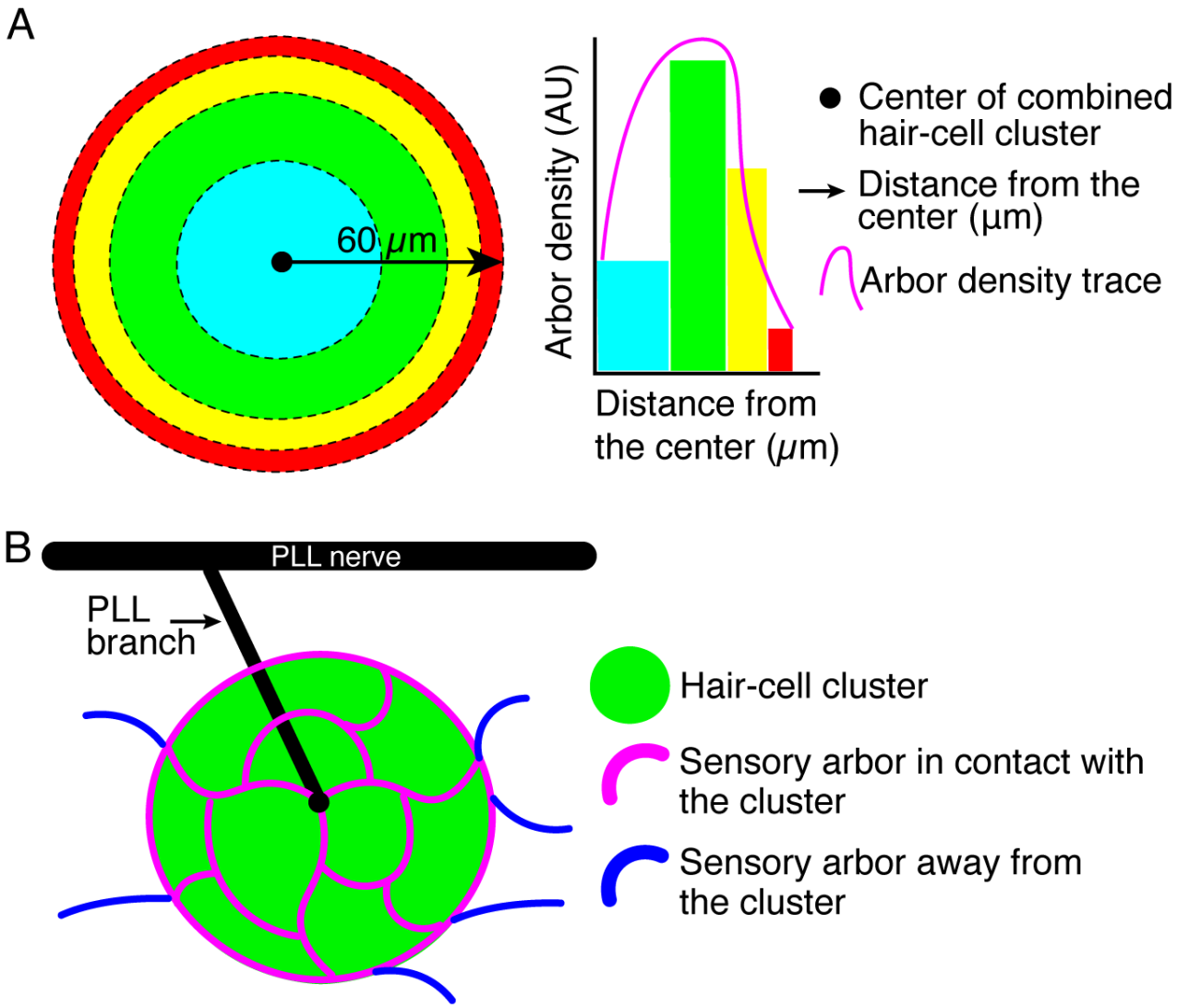

Figure 2—figure supplement 2. Quantification of sensory arbor distributions and contacts with hair cell clusters. (A) A schematic drawing of the combined hair cell cluster and surrounding region depicts concentric sections of equal area in distinct colors (cyan, green, yellow, and red). The arbor density is plotted as a histogram against the distance (black arrow) from the center (black circle) of the combined hair cell cluster. The histogram is represented as a density trace graph (magenta). (B) A schematic drawing of a posterior lateral-line neuromast depicts the posterior lateral-line (PLL) nerve (black), posterior lateral-line branch (black), the sensory arbors (magenta) that contact the hair cell cluster (green), and the sensory arbors that project away (blue) from the hair cell cluster.

812 **Video 2. Three-dimensional arborization patterns in control and *sema7a*$^{-/-}$ neuromasts.**

813 Lateral views depict three-dimensionally rendered combined skeletonized network traces from

814 27 control and 27 *sema7a*$^{-/-}$ mutant neuromasts.

815

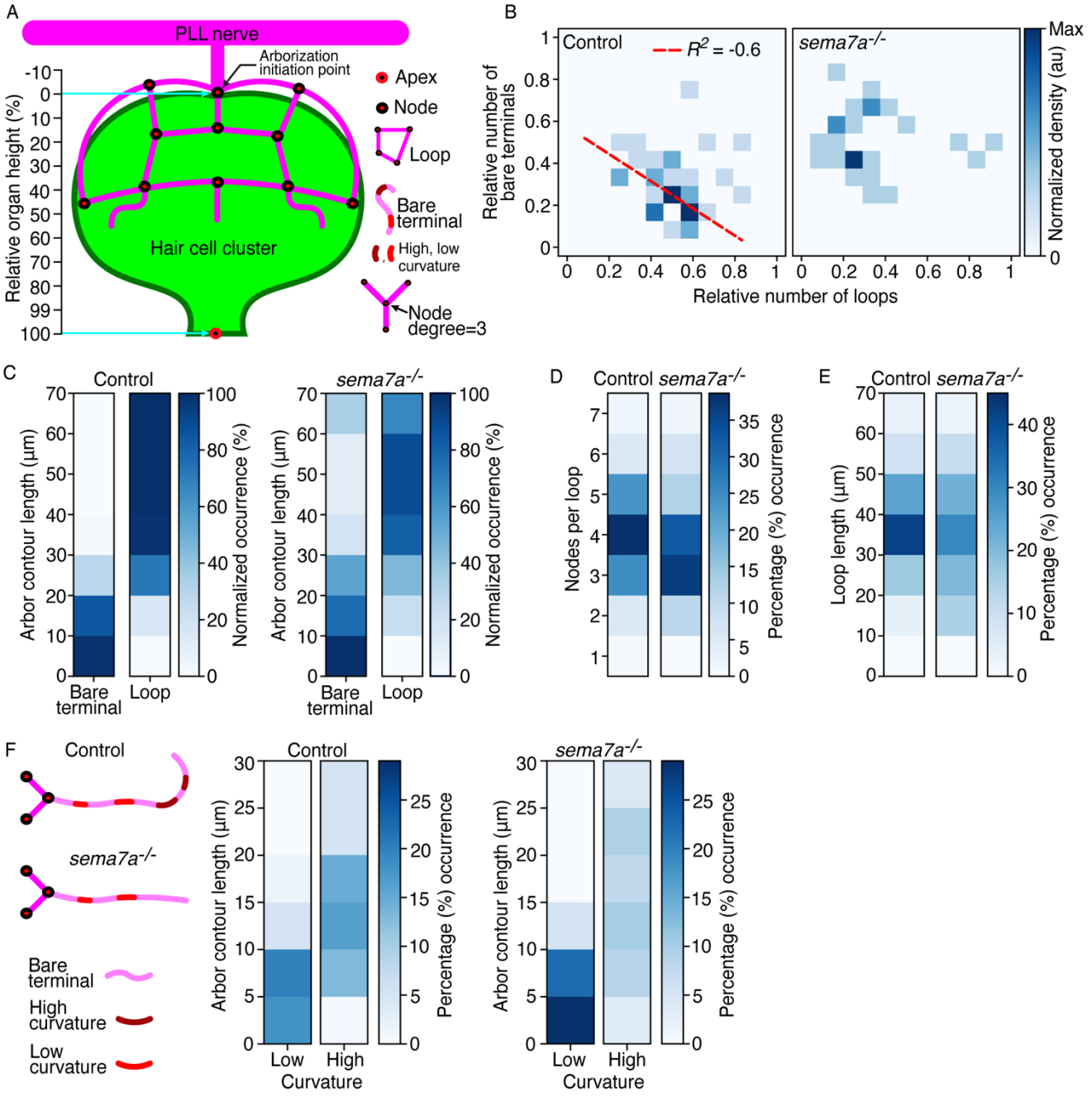

Figure 3. Sema7A patterns the topology of the sensory arbor network . (A) A schematic drawing of the combined hair cell cluster (green) and associated sensory axons (magenta) shows diverse topological features of the arborization network, including nodes, loops, bare terminals, node degree, and bare-terminal curvature. The apex is defined as the center of the hair bundle cluster and the base is denoted by the node from which the arborizations extends.

821 The relative organ height describes the position along the axis formed between the arborization
822 initiation point and the apex of the hair cell cluster. (B) The correlation between the relative
823 number of bare terminals and loops from 35 control neuromasts and 27 *sema7a*$^{-/-}$ neuromasts
824 at 4 dpf shows a negative correlation in the control but a scattered distribution in the mutants.
825 The same neuromasts were analyzed in the subsequent panels. R^2, correlation coefficient.
826 Dashed red line depicts the regression slope. (C) The relationship of contour lengths to bare
827 terminals and loops reveals reduced looping in the mutants. (D) Quantification of the number
828 of nodes per loop demonstrates a decrease in mutants. (E) Mutants in the same larvae manifest
829 a broader distribution of loop lengths. (F) A schematic diagram of the extending bare terminals
830 depicts regions of high and low curvature along the length of the arbor. The distributions of
831 bare terminals between low- and high-curvature groups show an enrichment of long, highly
832 curved arbors in the control and short, linear arbors in the mutants. Statistical analyses are
833 displayed in Table 1.

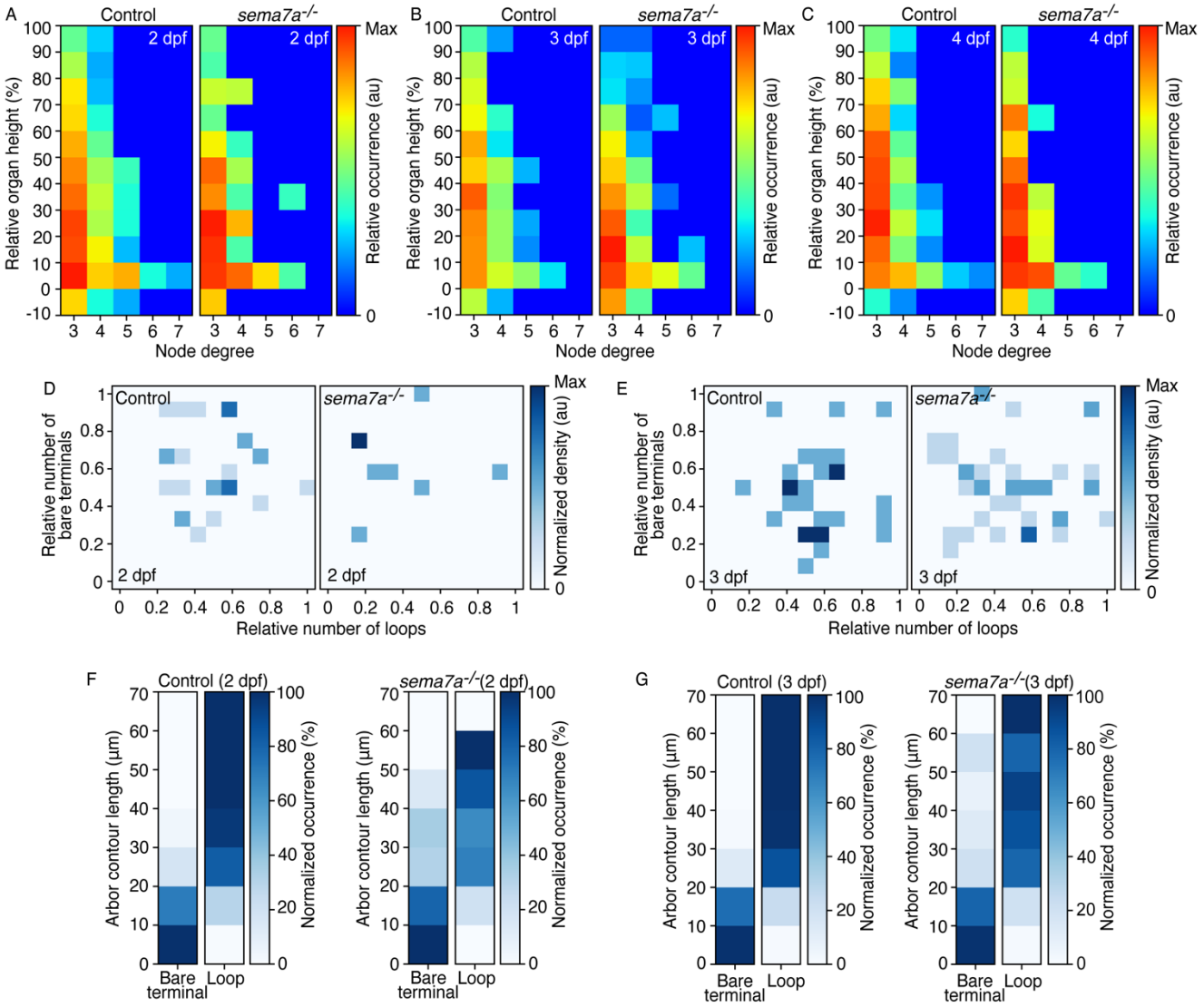

Figure 3—figure supplement 1. Quantification of topological features across developmental stages and genotypes. (A-C) The distribution of node degrees as a function of the height in hair cell clusters shows the difference in the network's hierarchical organization between control and *sema7a*$^{-/-}$ larvae. Nodes of low degree are commonly observed between genotypes across developmental stages (A, B), but their distribution along the cluster height became significantly different at 4 dpf (C), with nodes in control larvae localizing higher along the axis than in the mutants. In this and the following two panels, 33, 29, and 35 neuromasts were analyzed from 2 dpf, 3 dpf, and 4 dpf control larvae, respectively and 17, 53, and 27 neuromasts were analyzed from 2 dpf, 3 dpf, and 4 dpf *sema7a*$^{-/-}$ mutant larvae, respectively (D, E) The correlations between the relative number of bare terminals and loops from control

844 and *sema7a*$^{-/-}$ neuromasts reveal dispersive distributions at both 2 dpf (D) and 3 dpf (E) stages,
845 suggesting that the networks are undergoing reorganization and yet to adopt an ordered
846 topology. (F, G) In the distribution of arbors between bare terminals and loops with respect to
847 their contour lengths, mutants' arbors display significantly higher propensity to remain as bare
848 terminals compared to the controls at both 2 dpf (F) and 3 dpf (G) stages. The samples were
849 identical to those in the previous panel. Statistical analyses are displayed in Table 1.

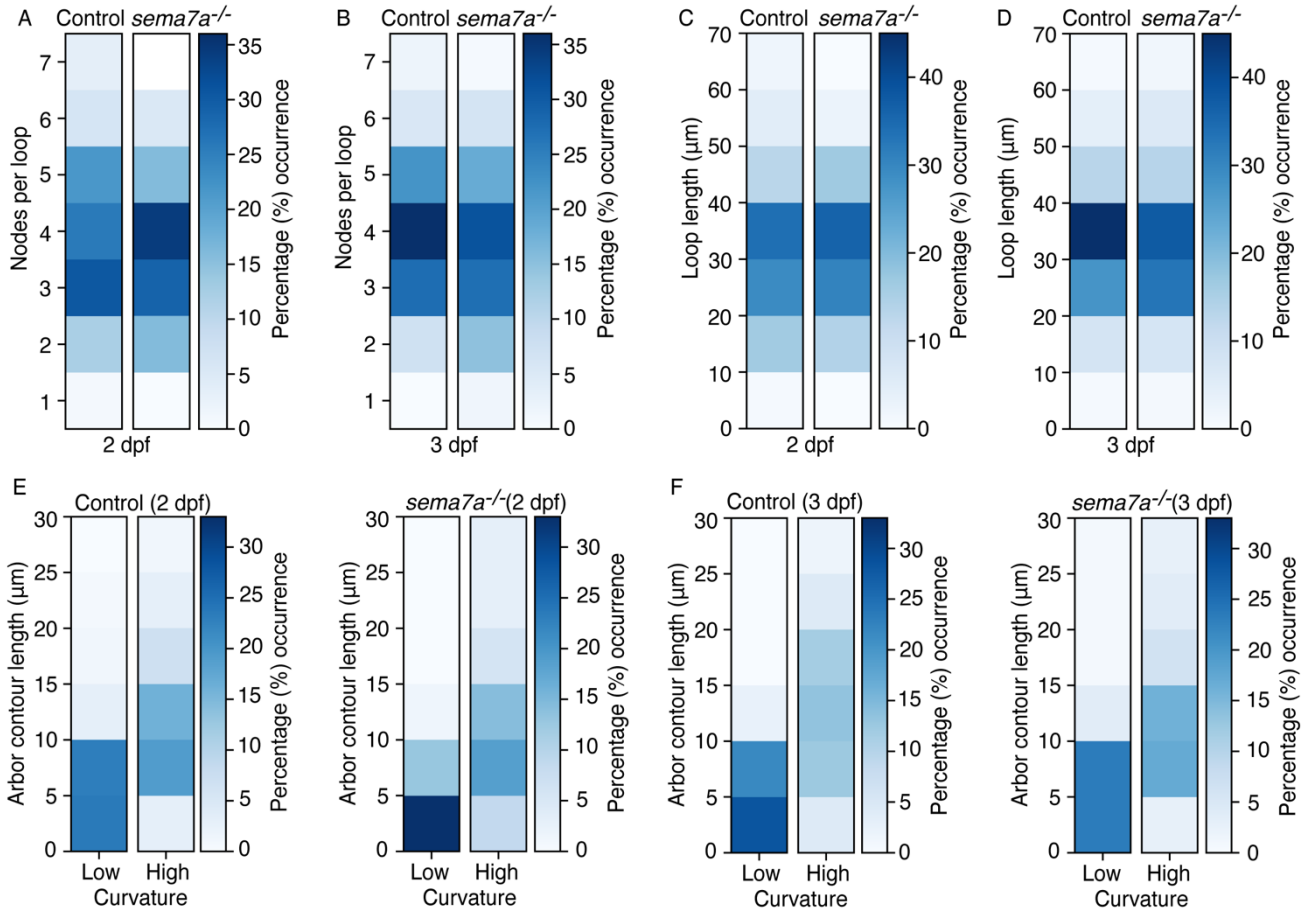

850 **Figure 3—figure supplement 2. Quantification of topological features between control**
851 **and *sema7a*$^{-/-}$ larvae across developmental stages.** (A, B) Quantifications of the number of
852 nodes per loop demonstrate a broader, but not significantly different, distribution in the mutants
853 than the controls at both 2 dpf (A) and 3 dpf (B). In this and the following panels, 33 and 29
854 neuromasts were analyzed from 2 dpf and 3 dpf control larvae, respectively and 17 and 53
855 neuromasts were analyzed from 2 dpf and 3 dpf *sema7a*$^{-/-}$ mutant larvae, respectively. (C, D)
856 Quantifications of loop lengths from the same larvae indicate a wider, but not significantly
857 different, distribution in the mutants than the controls at both 2 dpf (C) and 3 dpf (D). (E, F) The
858 distributions of bare terminals between low- and high-curvature groups from the same larvae
859 show higher occurrences of long, curved arbors in the control and short, linear arbors in the
860 mutants at both 2 dpf (E) and 3 dpf (F) stages. Statistical analyses are displayed in Table 1.

Height of node degrees	*p*-values (control vs *sema7a*$^{-/-}$)		
	2 dpf	3 dpf	4 dpf
Degree = 3	3.50E-01	1.05E-08*	1.68E-03*
Degree = 4	3.85E-01	7.11E-02	1.71E-03*
Degree = 5	4.60E-01	5.23E-01	4.40E-01
Bare terminals vs Loop	2 dpf	3 dpf	4 dpf
0 to 10 μm	3.84E-01	7.89E-01	2.11E-01
10 to 20 μm	3.50E-02*	3.92E-01	2.94E-02*
20 to 30 μm	2.28E-04*	2.63E-02*	3.82E-09*
30 to 40 μm	5.04E-59*	3.63E-25*	1.28E-33*
40 to 70 μm	———	———	———
Nodes per loop	5.06E-01	1.96E-01	3.50E-02*
Loop length	5.81E-01	2.71E-01	2.21E-02*
Distribution of bare terminal curvature	2 dpf	3 dpf	4 dpf
	4.23E-01	8.91E-01	1.99E-02*

Table 1. Statistical comparison between control and *sema7a*$^{-/-}$ larvae for topological features. One-sided Kolmogorov-Smirnov tests were used to assess the difference in node degree heights, nodes per loop, and loop lengths for control *versus sema7a*$^{-/-}$ neuromasts at 2 dpf, 3 dpf, and 4 dpf. In each of these cases, the difference in the distributions were not significantly different (*p*-values in red) between the control and the mutants at 2 dpf and 3 dpf but became significantly different (*p*-values in green) at 4 dpf. Chi-square tests were used to assess the difference in occurrences of bare terminals *versus* loops, as well as the occurrences of bare terminals with low *versus* high curvature. The distribution at 4 dpf shows significant difference between the control and the mutant larvae. The occurrence of significant differences at 4 dpf for diverse topological features suggest that Sema7A function is required to achieve an ordered network topology at a mature stage. Thirty-three, 29, and 35 neuromasts were

873 analyzed from 2 dpf, 3 dpf, and 4 dpf control larvae, respectively, and 17, 53, and 27
874 neuromasts were analyzed from 2 dpf, 3 dpf, and 4 dpf *sema7a*$^{-/-}$ mutant larvae, respectively.
875 * signifies $p < 0.05$.
876

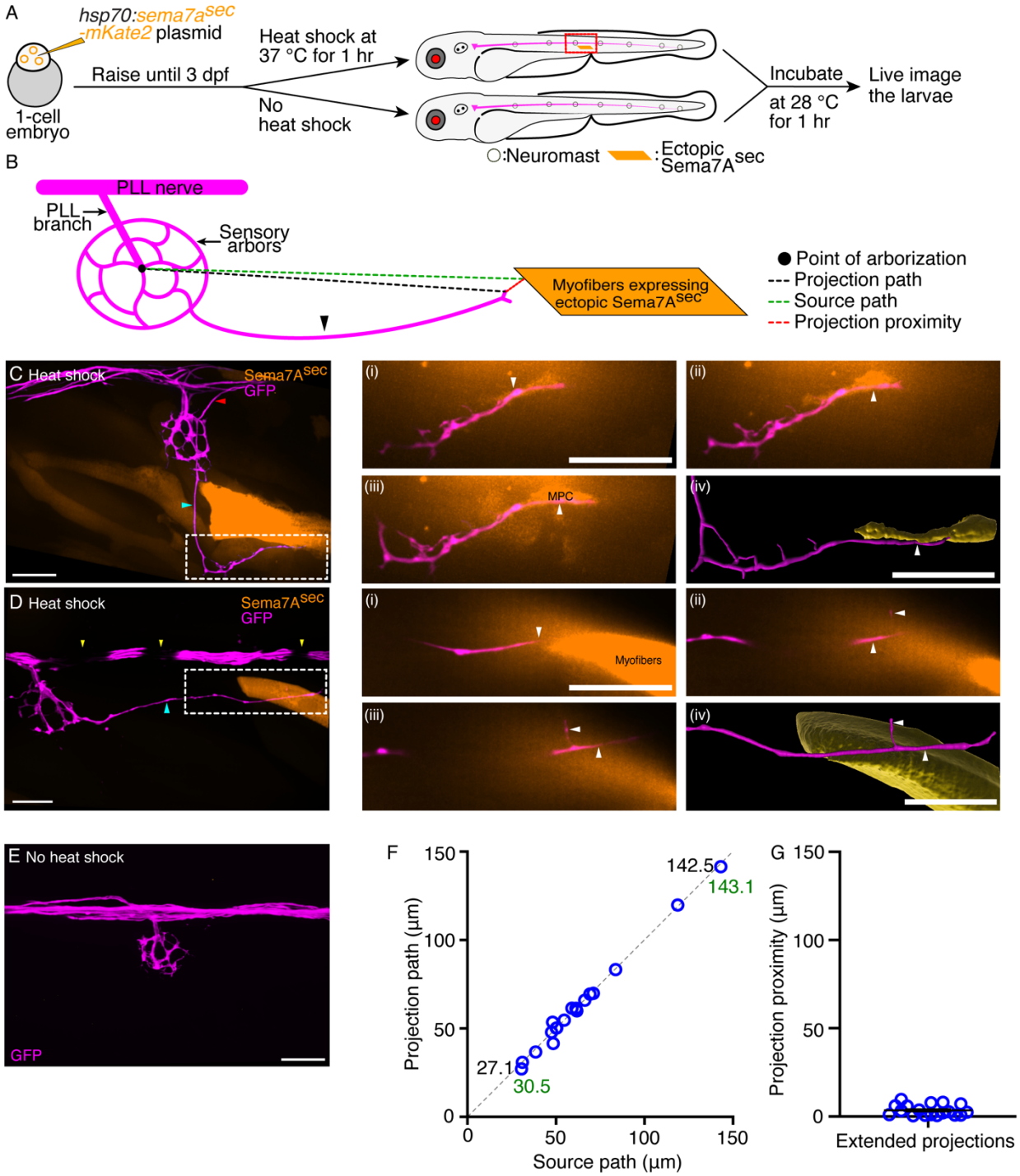

877 **Figure 4. Ectopic Sema7A^sec diffusive cue provides neural guidance *in vivo*.** (A) A
878 diagrammatic overview depicts the generation of a transgenic animal that expresses the
879 Sema7A^sec protein ectopically under the control of a thermally inducible promoter. Larvae with
880 ectopic myotomal-integration near the network of sensory arbors (red line) were imaged to

881 analyze arbor morphology. (B) A schematic drawing of a sensory arbor from a heat-shocked
882 larva depicts an extended axonal projection (arrowhead) that reaches toward the myofibers
883 expressing the ectopic Sema7A^{sec} protein. Parameters that quantitate the accuracy of the
884 extended axonal projections toward the ectopic Sema7A^{sec} sources are denoted. (C) In a
885 micrograph of an ectopically expressing Sema7A^{sec} (orange) larva, the sensory arbor
886 (magenta) extends two aberrant axonal projections. One elongates (cyan arrowhead) along
887 the somite boundary to reach and contact an ectopically integrated muscle progenitor cell
888 (white dashed line) and the other (red arrowhead) reenters the posterior lateral-line nerve while
889 following a second ectopic source. The through-focus scans (i–iii) from the epidermis to the
890 dermomyotome and the three-dimensional (3D) surface reconstruction (iv) reveal the intimate
891 contact between the aberrant sensory arbor (arrowheads) and the muscle progenitor cell. (D) In
892 a micrograph of an ectopically expressing Sema7A^{sec} (orange) larva, the sensory arbor
893 (magenta) extends a single aberrant axonal process (cyan arrowhead) to reach ectopically
894 integrated myofibers (white dashed line). The through-focus scans (i–iii) from the epidermis to
895 the dermomyotome and the 3D surface reconstruction (iv) reveal the proximal association of
896 the aberrant sensory arbor (arrowheads) to the myofibers. Melanocytes (yellow arrowhead)
897 along the horizontal myoseptum intermittently block the visibility of the lateral-line nerve. (E) An
898 injected, but not heat-shocked, control larva does not express ectopic Sema7A^{sec} and does not
899 show aberrant projection from the sensory arbor. (F) A plot demonstrates the accuracy of 18
900 extended axonal arbors in finding ectopic Sema7A^{sec} sources. Each circle represents a single
901 ectopic integration event. The two pairs of numbers represent the minimal and maximal lengths
902 of the projection path (black) and its corresponding source path (green). (G) A plot quantitates
903 the distribution of projection-proximity length from 18 ectopic integration events. MPC, muscle
904 progenitor cell; scale bars, 20 μm; means ± SEMs.
905

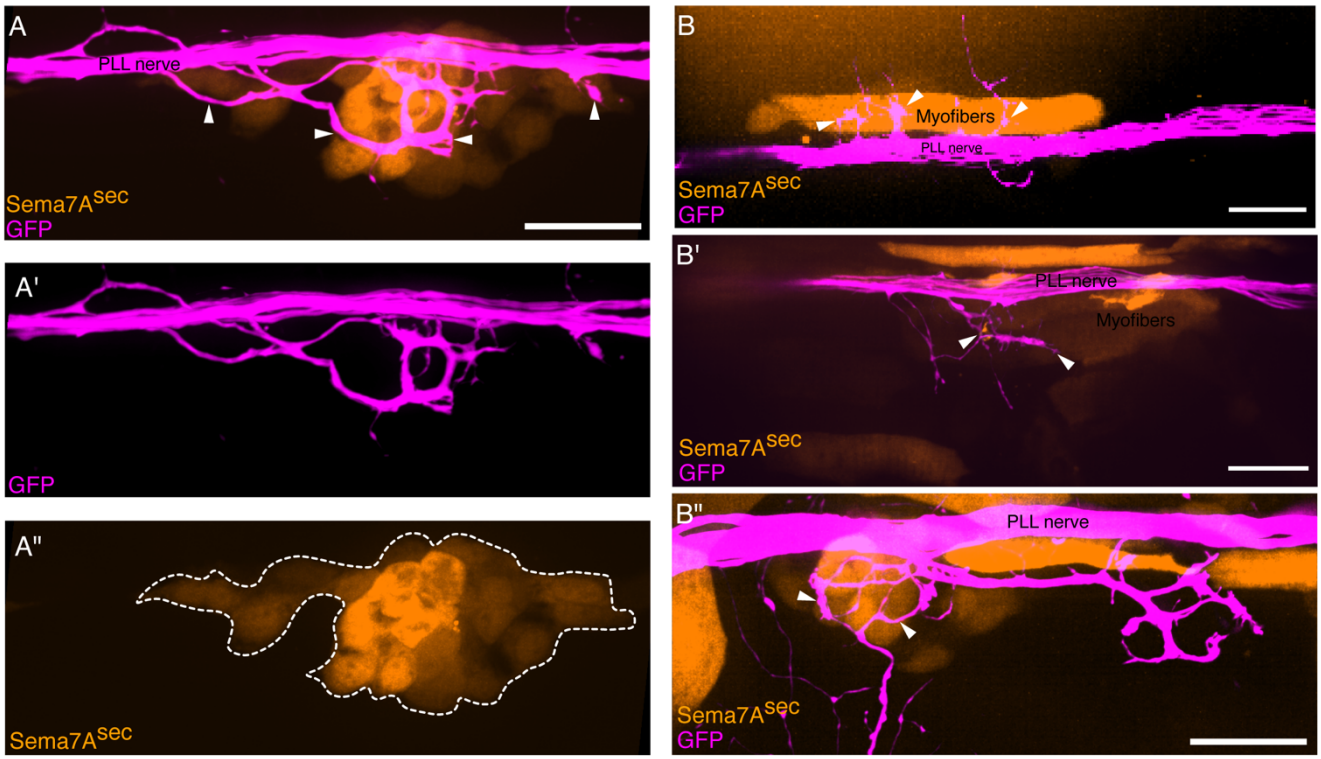

Figure 4—figure supplement 1. Ectopic Sema7A^{sec} diffusive cues induce aberrant neural arborizations. (A-A") In a micrograph of an ectopically expressing Sema7A^{sec} (orange) larva, the sensory arbors (magenta) extend multiple aberrant axonal projections (arrowheads) that reenter the lateral-line nerve while following an ectopic Sema7A source. Maximal-intensity projections of the sensory arbors and the ectopically expressing Sema7A cells (white dashed line) are shown in A' and A", respectively. (B-B") Micrographs depict three individual incidents of ectopic *sema7a^{sec}* (orange) integrations that occurred distant from neuromasts. In each case, a set of myofibers expresses the ectopic Sema7A^{sec} protein that induces neurite extensions (arrowheads) from the lateral-line nerve (magenta) toward itself. Scale bars, 20 μm.

915 **Video 3. Sensory axonal projections contact an embryonic muscle progenitor cell**
916 **expressing Sema7A^{sec}.** A through-focus scan of a 3 dpf larva depicts a muscle progenitor
917 cell in the dermomyotome that expresses the ectopic Sema7A^{sec} (orange) and the sensory
918 axonal projection (magenta) that makes intimate contact with it. Scale bar, 20 μm.

919 **Video 4. Volumetric surface reconstruction of a sensory arbor and an embryonic muscle**
920 **progenitor expressing Sema7A^{sec}.** Reconstruction of the muscle progenitor cell (orange) at
921 3 dpf reveals its intimate association with an attracted sensory arbor (magenta).

922 **Video 5. Sensory axonal projections remain in proximity to myofibers expressing**
923 **Sema7A^{sec}.** A through-focus scan of a 3 dpf larva depicts mature myofibers expressing
924 exogenous Sema7A^{sec} deep in the myotome (orange) and the sensory axonal projection
925 (magenta) that remains nearby.

926 **Video 6. Volumetric surface reconstruction of a sensory arbor and the mature myofibers**
927 **expressing Sema7A^{sec}.** Reconstruction of mature myofibers expressing ectopic Sema7A^{sec}
928 (orange) at 3 dpf shows their close association with the attracted sensory arbors (magenta).

929 **Video 7. Aberrant axonal projections reenter the lateral-line nerve while following an**
930 **ectopic Sema7A^{sec} source.** A through-focus scan of a 3 dpf larva depicts cells expressing
931 exogenous Sema7A^{sec} (orange) that guides the aberrant sensory axonal projection (magenta)
932 back into the lateral-line nerve. Scale bar, 20 μm.

933 **Video 8, 9, and 10. Ectopic Sema7A^{sec} expression induces aberrant neurite projections**
934 **from the lateral-line nerve.** Through-focus scans of 3 dpf larvae depict three individual
935 incidents of ectopic *sema7a^{sec}* (orange) integrations that occurred distant from the neuromasts.
936 In each case, myofibers express ectopic Sema7A^{sec} protein that attracts neurite extensions
937 (arrowheads) from the lateral-line nerve (magenta). Scale bars, 20 μm.

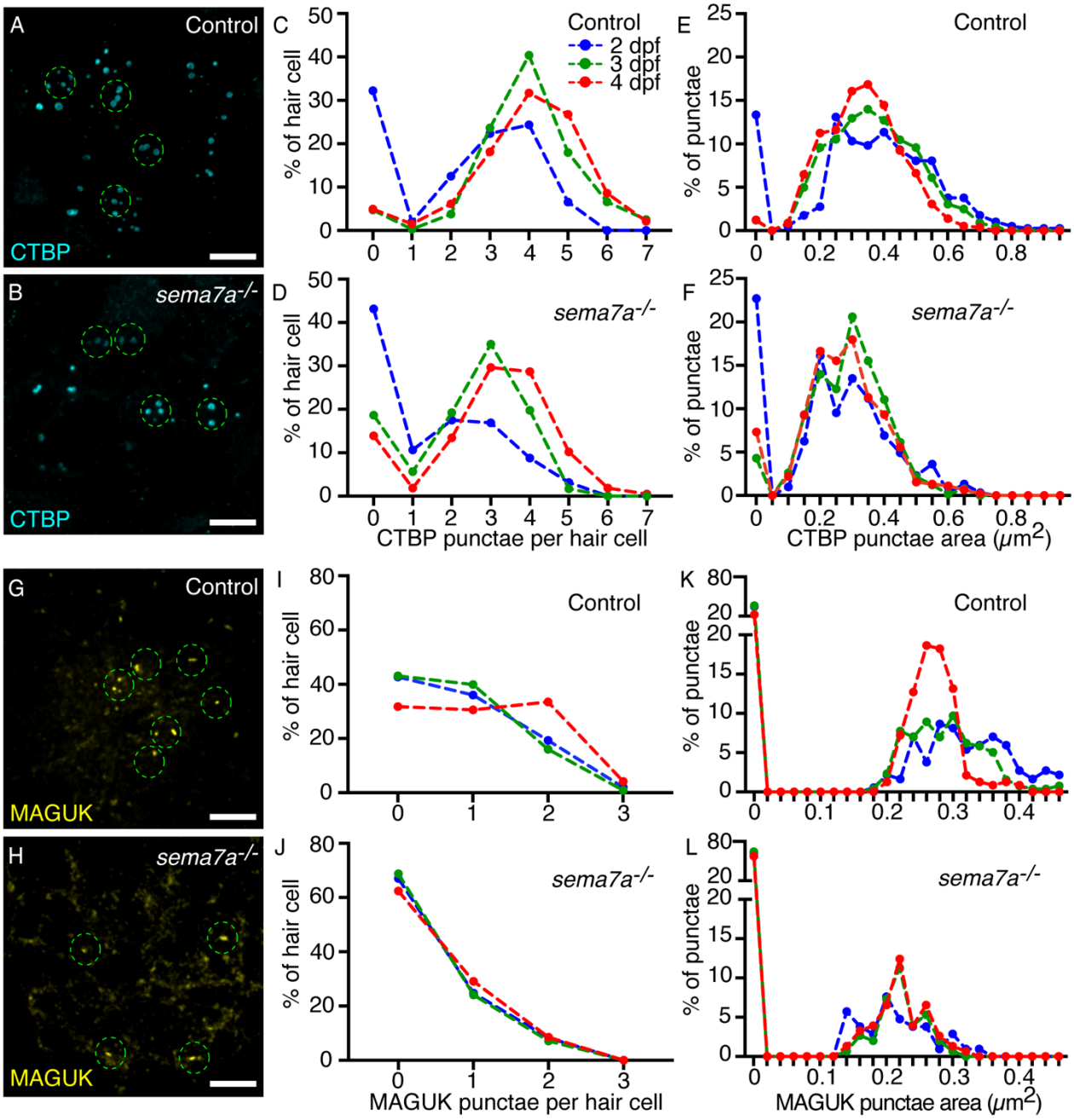

938

939 **Figure 5. Sema7A deficiency impairs synaptic assembly.** (A,B) Maximal-intensity
940 projections of micrographs from a control and a *sema7a*$^{-/-}$ neuromast depict the presynaptic
941 aggregates marked by CTBP (cyan). The approximate hair cell basal region is outlined by
942 dashed green circles. (C-F) Plots quantitate the numbers of presynaptic aggregates (C,D) and
943 their areas (E,F), in each hair cell across developmental stages. One hundred and fifty-two,
944 317, and 325 hair cells were analyzed from 2 dpf, 3 dpf, and 4 dpf control larvae, respectively.

945 One hundred and sixty, 216, and 177 hair cells were analyzed from 2 dpf, 3 dpf, and 4 dpf
946 *sema7a*$^{-/-}$ mutant larvae, respectively. (I,J) Maximal-intensity projections from micrographs of
947 a control and a *sema7a*$^{-/-}$ neuromast depict the postsynaptic aggregates marked by MAGUK
948 (yellow). The approximate hair cell basal region is outlined by dashed green circles. (K-N) Plots
949 quantitate the numbers of postsynaptic aggregates (K,L) and their areas (M,N), in each hair
950 cell across developmental stages. One hundred and fifty, 218, and 167 hair cells were analyzed
951 from 2 dpf, 3 dpf, and 4 dpf control larvae, respectively. Ninety-seven, 141, and 141 hair cells
952 were analyzed from 2 dpf, 3 dpf, and 4 dpf *sema7a*$^{-/-}$ mutant larvae, respectively. Scale bars,
953 5 μm.

954

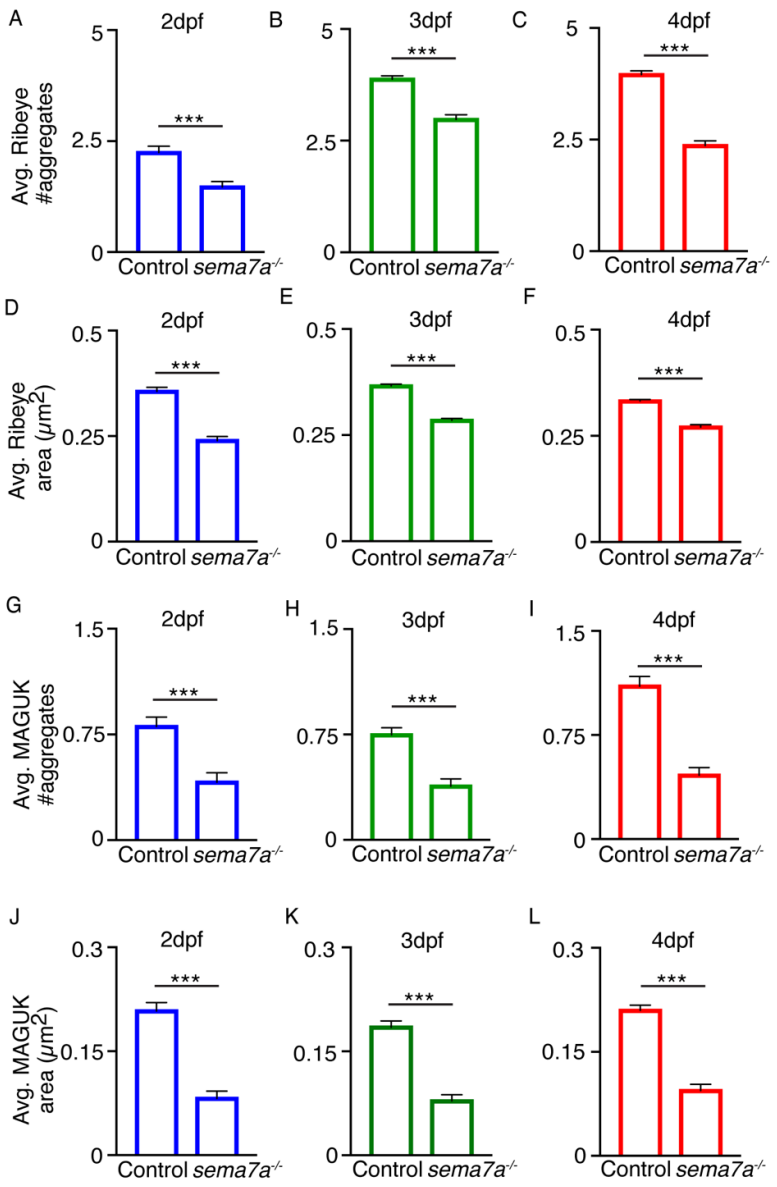

955 **Figure 5—figure**

956 **supplement 1. *sema7a*$^{-/-}$ mutants display impaired synaptic assembly.** (A-F) The plots
957 quantitate the average numbers and areas of presynaptic aggregates from control and *sema7a*$^{-}$
958 $^{/-}$ neuromasts. Significant decreases in the numbers and areas of presynaptic aggregates are
959 observed across development. Three hundred and forty-one, 1229, and 1286 presynaptic
960 aggregates were analyzed from 2 dpf, 3 dpf, and 4 dpf control larvae, respectively. Two
961 hundred and thirty-five, 643, and 419 presynaptic aggregates were analyzed from 2 dpf, 3 dpf,
962 and 4 dpf *sema7a*$^{-/-}$ mutant larvae, respectively. (G-L) The plots quantitate the average

963 numbers and areas of postsynaptic aggregates from control and *sema7a*$^{-/-}$ neuromasts.
964 Significant decreases in the numbers and areas of postsynaptic aggregates occurred during
965 development. Three hundred and ninety-seven, 1243, and 1300 postsynaptic aggregates were
966 analyzed from 2 dpf, 3 dpf, and 4 dpf control larvae, respectively. Three hundred and four, 651,
967 and 451 postsynaptic aggregates were analyzed from 2 dpf, 3 dpf, and 4 dpf *sema7a*$^{-/-}$ mutant
968 larvae, respectively. Means ± SEMs; *** implies $p < 0.001$.

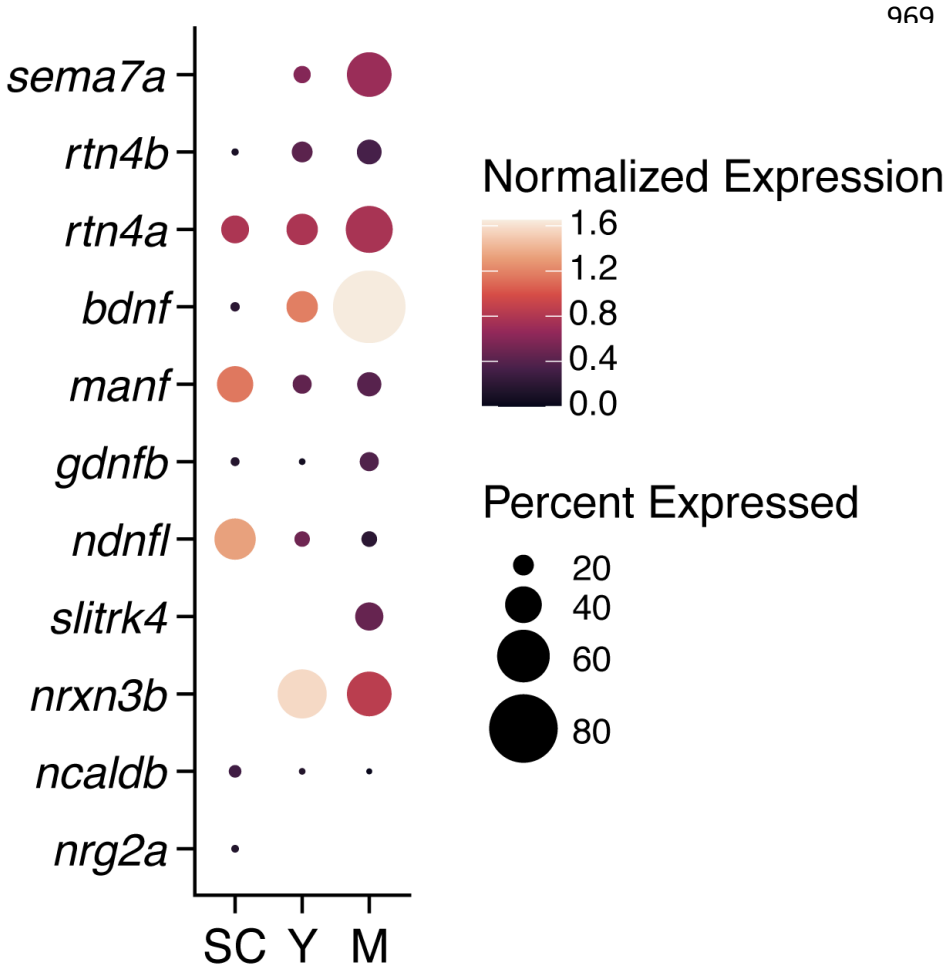

Figure 6. Expression of diverse neural guidance cues in developing neuromasts. Analysis of single cell RNA-sequencing data (9) shows the expression of multiple neural guidance genes that are expressed across young hair cells (Y), mature hair cells (M), and support cells (SC). Dot sizes and colors signify the proportion of cells in each cluster that express a gene and the average strength of expression (log[(counts/10,000) +1]), respectively.